Journal International Perforating Forum

A Journal For The International Perforating Industry

VOL.3, ISSUE NO.1/FEBRUARY 2020

ARTICLE 1. NUMERICAL SIMULATION FOR NEAR BOREHOLE FLUID DYNAMICS AT PERFORATION TUNNEL

ARTICLE 2. ANALYSIS OF NEW RP 67 RECOMMENDED SAFETY DISTANCES FOR 50-OHM RESISTORIZED AND RF-SAFE DETONATORS

ISSN 2471-9374

JIPF TECHNICAL EDITORS

The Journal of the International Perforating Forum would not be possible without a dedicated network of industry experts to serve as peer reviewers. We gratefully acknowledge the following individuals who have agreed to serve as technical editors for JIPF.

Achim Pabst	*DynaEnergetics*
Adam Dyess	*Hunting Titan*
Alex Procyk	*Consultant*
Andrew Werner	*Schlumberger*
Anthony Nguyen	*Conoco Phillips*
Bill Harvey	*Baker Hughes*
Bill Myers	*Baker Hughes*
Bob Haney	*Consultant*
Brenden Grove	*Halliburton*
Carlos Bauman	*Schlumberger*
Chip Levine	*YellowJacket*
Chris Chow	*Consultant*
Chris Hoelscher	*Halliburton*
Chris Sokolove	*Hunting Titan*
Christian Eitschberger	*DynaEnergetics*
Clinton Quattlebaum	*Halliburton*
Dario Lattanzio	*ETA*
Dave Ditty	*Austin Powder*
Dave Leidel	*Directed Energetic Systems*
David Atwood	*SLB (Atwood Eng)*
David Ayre	*BP*
David Cuthill	*GEODynamics*
David Smith	*Hunting Titan*
David Underdown	*Consultant*
Dennis Baum	*LLNL*
Eliana Mandujano	*Imporio Media*
Gerald Craddock	*Halliburton*
Jacob McGregor	*Halliburton*
James Barker	*Halliburton*
Jason McCann	*Baker Hughes*
Jason Metzger	*Halliburton*
Jim Gilliat	*Baker Hughes*
Joern Loehken	*DynaEnergetics*
John Carminati	*Shell*
John Rodgers	*Starboard*
Lang Zhan	*Shell*
Larry Albert	*Allied Horizontal WL*
Larry Behrmann	*Consultant*
Lian McNelis	*DynaEnergetics*
Mark Brinsden	*Vektor Energy*
Matthew Clay	*Owen*
Meng Yu	*Shell*
Niall Fleming	*Statoil*
Oliver Han	*Hunting Titan*
Parry Hillis	*Baker Hughes*
Rajani Satti	*Baker Hughes*
Ryan White	*Baker Hughes*
Shaun Geerts	*Owen*
Stuart Wood	*Halliburton*
Thilo Scharf	*DynaEnergetics*
Tim LaGrange	*Owen*
Dan Pratt	*Owen*

CONTENTS

A Word From the JIPF Executive Editors

Welcome to the fourth issue of the Journal of the International Perforating Forum. This issue follows another busy year within the industry, as the role of North American unconventionals continues to evolve in the context of the global energy picture. Although North America land activity has grown to represent a majority of perforating work (in terms of number of jobs, charges, etc.), offshore and international activity is picking up as many projects have been deemed viable at "lower for longer" commodity prices.

John Carminati

In this issue of the Journal we highlight two important and linked areas of study. The first is modeling. Rigorous modeling establishes well production realizations. These influence many outlfow completion and facility factors such as tubing size, separator size, flowline size, timing of artificial lift, etc.; in addition to establishing a revenue stream prediction. Modeling also impacts the investment required to complete the well by enabling comparison of charge performance and assessing the influence of other aspects of the perforating operation, such as propellants. Once these realizations justify a completion, the link to safety is established which leads us to our second contribution. A completion is only viable if it can be installed safely. With regards to perforating, safety considerations generally focus on ensuring that the perforating system functions only when intended – and reliably when intended. Many safety advances in recent years have been driven by the pursuit of achieving these 2 goals in the context of high-efficiency plug-and-perf operations.

Brenden Grove

In addition to the featured technical articles, this issue also highlights recent and future industry activities – in particular the well-attended North American Perforating Symposium (NAPS) – the first ever hosted in the DFW metroplex.

We hope you find the content of this is useful and interesting. And we sincerely thank the authors, reviewers, and contributors who have made this issue possible.

John Carminati and Brenden Grove
JIPF Executive Editors

Message from the IPFC Board of Directors

Welcome to all our IPFC and JIPF Stakeholders! We are sure you will enjoy this excellent fourth edition of the JIPF. The editorial team has done a fantastic job in creating this edition, for which the Board of Directors are truly thankful.

2019 has been a busy year for our staff and organizing volunteers. Alphie Wright and his team put together the first regional North American Perforating Symposium (NAPS) in Arlington TX, over the 5-6th of August, which was very successful, and well attended. During NAPS, the IPFC held its Annual Meeting, where we voted to add Alphie Wright as a fifth Director. This will be effective as soon as we can amend the IPFC bylaws. Additionally, Larry Albert and Matthew Clay graciously agreed to co-chair the organizing committee for the 2020 Symposium in Galveston TX (May 12-13th 2020). So save the date, and begin thinking about your abstracts for this event!

We were also pleased to see in October that the 3rd edition of the API Recommended Practice 67, Oilfield Explosive Safety was published. While not directly an IPFC matter, RP 67 was being worked on by many of us, and is a culmination of ~6 years of concerted effort to improve the safety of our industry. I would like to personally thank each and every one of you who participated in this effort, on a job well done!

David Ayre
Vice President, International Perforating Forum Co.

On behalf of the Directors of the IPFC,
Mark Brinsden, James Barker, John JW Segura, Alphie Wright


David Ayre


Mark Brinsden


James Barker


John JW Segura


Alphie Wright

Perforating Safety

I would like to thank Frank Preiss who has been the IPF Safety Chairman since its inception. His excellent performance and dedication to our industry has been noticed by his peers, and we wish him well with his future endeavors.

As the newly selected Safety Chairman, I encourage all within our industry to strive toward ZERO perforating accidents. We must maintain these high safety goals for the benefit of our colleagues, friends, and loved ones.

As Frank has explained in past articles, our purpose within the IPFC is to help the industry prevent unintentional detonation of explosives. Should there be an incident or a near miss, we must be prepared to report this in order to bring awareness to others in our industry. The IPFC ensures that names of people and companies are kept in strict confidence. We only report the incident or near miss, so that the readers may decide what actions need to be taken in order to prevent similar incidents from recurring. The IPF only reports; it does not provide guidance or solutions.

Please submit incidents or near misses by going to our website at www.perforators.org.

Alphie Wright
Safety Chair, IPF


Alphie Wright

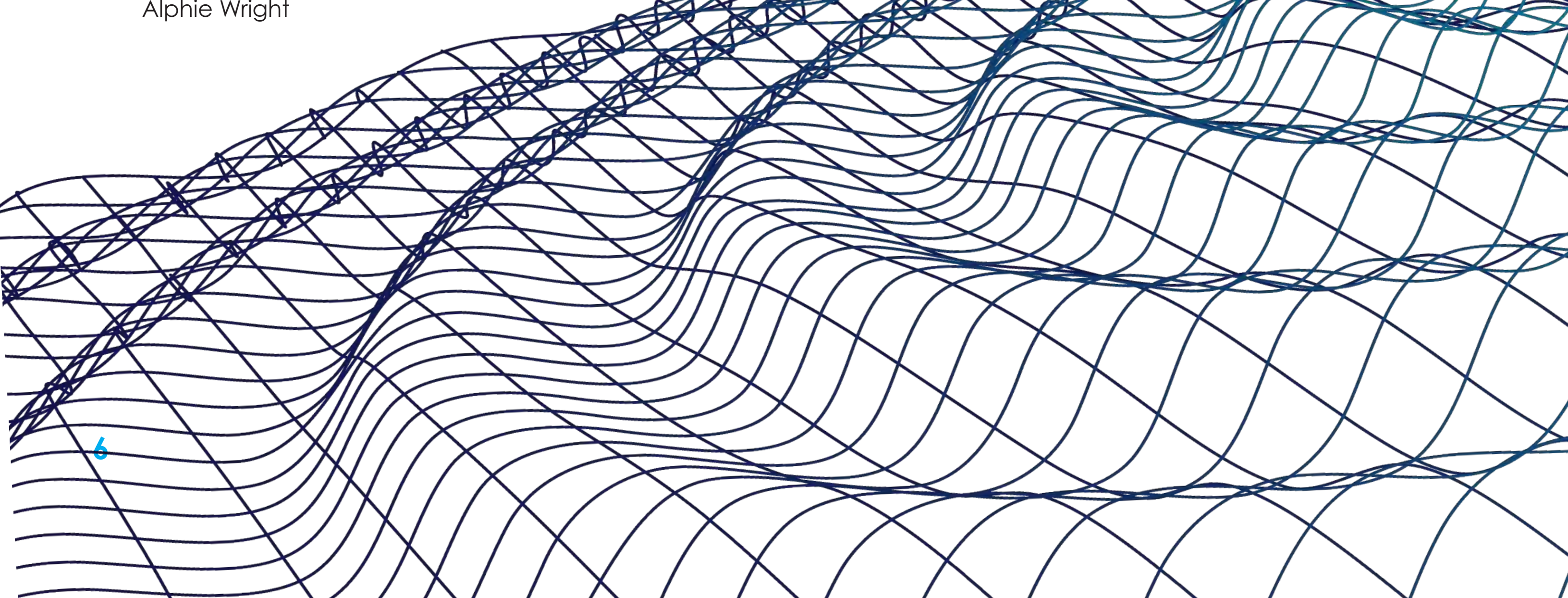

Continuing Education

In 2016 the IPFC began the Continuing Education initiative with the mission to disseminate knowledge across the perforating community by providing professionals an opportunity to boost their technical knowledge.

Today we have quality perforating resources available at the website including Papers and Articles on different topics such as: Perforating Dynamics, Perforating Testing, Perforating Modelling, Productivity Improvements, Explosives Safety and Operational Efficiency Improvements. I encourage you to visit the continuous education website for appreciation of this material. Let me know if any feedback on any other topics you would like to see on the website. (https://perforators.org/continuing-education/)

The Continuing Education Chair is now looking at expanding its reach by implementing Monthly Webinars on perforating topics. The first webinar entitled "Using The Revised And Improved API19B To Enhance Your Perforating Performance", presented by Mark Brinsden, Vektor Energy Inc., President of the IPFC was held during January 2020 and is now available on the website's continuing education section. Would you like to share your knowledge with the community? The committee is looking for presenters. Please contact us at education@perforators.org

Carlos Guedes,
Continuing Education Chair, IPF

Carlos Guedes

Regional Updates

North America

Planning for IPS 2020 is underway. The event is set for May 12-13 at the Moody Gardens Hotel and Convention Center in Galveston, TX. Committee assignments have been made, and we have been actively working the project since November. We are looking forward to a great conference. A high priority for this event will be an increase in E&P company participation. Ideas to help us achieve this objective are most welcome. Please put the event on your calendars and consider actively participating by submitting a technical abstract, volunteering, or both!

Matt Clay, Corelab
Larry Albert, Horizontal Wireline Services
IPS 2020, USA Co-Chairs

IPS 2020
INTERNATIONAL PERFORATING SYMPOSIUM

Europe

Following the 2019 IPFC meeting in Dallas, the feasibility of organizing a regional perforating symposium in Europe during 2020/21 was investigated.

After discussions with key individuals within operator and service organizations, it has been determined that a full symposium would be challenging to support at this time, due to uncertainties around sponsorship commitments as well as content submissions from potential authors.

An alternative approach is therefore proposed, which involves collaborating with like-minded organizations to organize a joint event. Specifically, the Institute of Explosives Engineers (IEE), located in the UK are now holding well established and well attended technical conferences and one day workshops, focused on explosives matters, including oil and gas matters. Considering the established links between members of the IFPC and the IEE (and similar bodies in the USA), organizing a joint event could easily be pursued.

Andy Pettitt
Dullan Resources Limited, UK

Asia Pacific

The next Asia Pacific Perforating Symposium (APPS) is currently being planned for 2021 in Kuala Lumpur, Malaysia. If you would like to participate on the next committee, please contact any of the IPFC Executive Committee or myself. Previous symposia in 2011, 2013 and 2018 showed the strong interest in perforating within the Asia Pacific region. Please browse the photos https://perforators.org/apps-2018-photos/ and the presentations https://perforators.org/ips-presentations/.

John P Davidson
APPS Committee 2011, 2013, 2018

Middle East

The next Middle East / North Africa Perforating Symposium (MENAPS) is being planned for November 2020. Stay tuned for further information.

Hanaey Ibrahim
PDO, Oman

ARTICLE 1.

NUMERICAL SIMULATION FOR NEAR BOREHOLE FLUID DYNAMICS AT PERFORATION TUNNEL

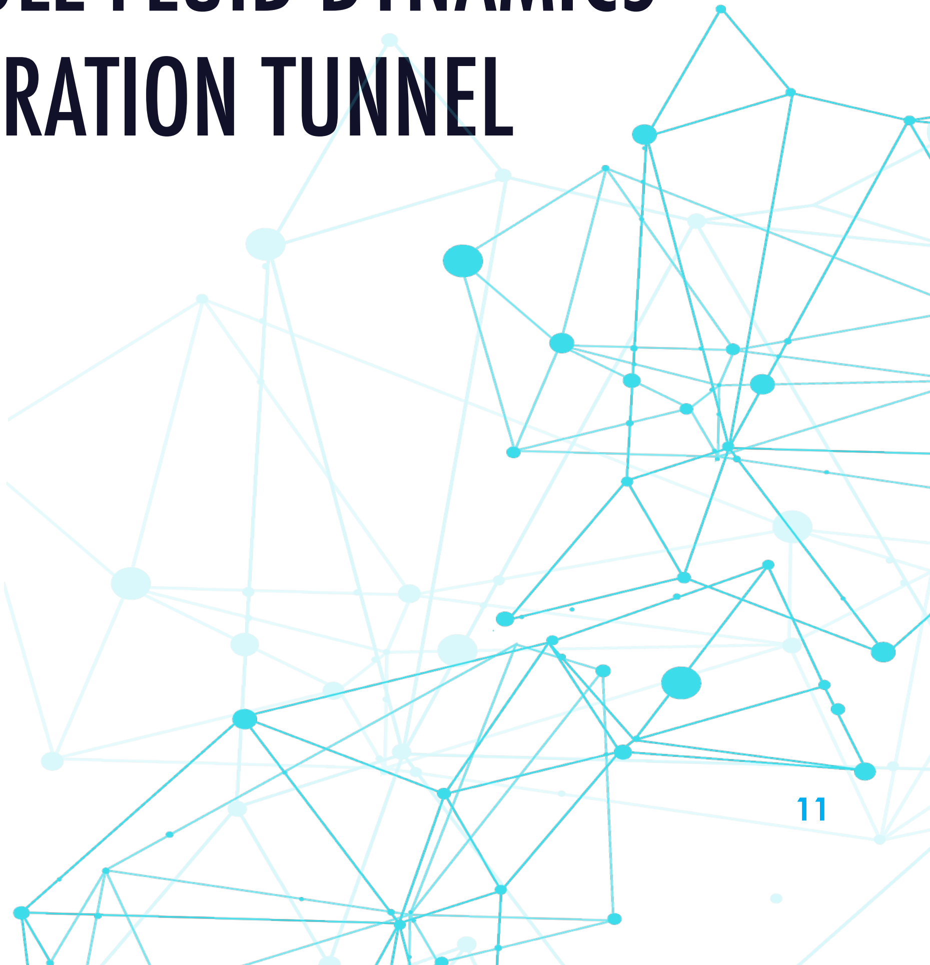

COVER SHEET

Numerical simulation for near borehole fluid dynamics at perforation tunnel

Authors:
Carlos Vega Ortiz, University of Utah
John McLennan, University of Utah
Ian Walton, Energy and Geoscience Institute

Author Biographies:

Carlos Vega is originally from San Marcos, Hgo, Mexico. He received the B. Degree in Physics Engineering from the Instituto Tecnologico y de Estudios Superiores de Monterrey in 2003, and MS in Petroleum Engineering from the University of Utah in 2016. Experienced in the oil and gas industry working for 11 years as reservoir evaluation wireline engineer and manager for Schlumberger in various assignments including Mexico, North Sea, Libya, and Turkey. Currently is pursuing a Ph.D. degree in Chemical Engineering at the University of Utah, focusing on Reservoir Engineering on Unconventional plays in Mexico. Carlos is Holder of Hydrocarbons grant by Mexico's Secretary of Energy and CONACYT.

John McLennan has been a USTAR Associate Professor in the Department of Chemical Engineering at the University of Utah since October 2009. He has been a Senior Research Scientist at the Energy & Geoscience Institute and an Adjunct Professor in the Department of Civil Engineering at the University of Utah, since January 2008. He has a Ph.D. in Civil Engineering from the University of Toronto, awarded in 1980. He has more than thirty-five years of experience with petroleum service and technology companies. He worked nine years for Dowell Schlumberger in their Denver, Tulsa, and Houston facilities. Later, John was with TerraTek in Salt Lake City, Advantek International in Houston, and ASRC Energy Services in Anchorage. He has worked on projects concerned with subsurface energy recovery (hydrocarbon, geothermal) in a variety of reservoir environments, throughout the world.

Dr. Ian C Walton is a Senior Research Scientist in the Energy and Geoscience Institute at the University of Utah and is also an Adjunct Professor in the Department of Chemical Engineering. He holds a Ph.D. in Applied Mathematics from the University of Manchester and a B.Sc. in Mathematics from University College London. He has a total of 11 years of academic experience between Imperial College London, and UCLA, where he was a Visiting Professor. Before joining EGI in 2010, he accumulated 25 years of oil industry experience beginning with BP Research in Sunbury and continuing at various Schlumberger locations including Schlumberger Cambridge Research, Dowell Tech Center, Tulsa, Perforating Research in Rosharon, Texas and the Regional Technology Center for Unconventional Gas in Dallas. He currently specializes in fluid flow and production analysis from shale reservoirs. He has published more than 70 technical papers, has been awarded eight patents and was appointed SPE Distinguished Lecturer for 2016-2017.

Numerical simulation for near borehole fluid dynamics at perforation tunnel

Vega-Ortiz, Carlos, University of Utah, **McLennan, John**, University of Utah, **Walton, Ian** Energy and Geosciences Institute

Abstract:

Perforation with shaped charges is the most common technique to establish a hydraulic pathway between the newly cased-and-cemented wellbore and the formation which may be a producer or an injector. During perforation, a low permeability 'crushed zone' is formed around perforation tunnels. This damaged region drastically reduces deliverability. Underbalanced perforating, surging, and acidizing are among strategies implemented by operators – with or without a clear understanding of the possibility for success – for reducing skin damage associated with this aspect of perforating.

This study uses a self-developed numerical analysis tool to evaluate the dynamics and pressure transient behavior of flow through the crushed zone, and the effects on porosity and permeability from treatments such as hydraulic fracturing and acidizing. The main inputs for the numerical simulation are simplified geometry and properties of the perforation(s), two-phase relative permeability relationships, petrophysical properties and texture of the rock (represented by a grid cell of predetermined porosity and permeability). The simulations have low computational overhead and enable multiple simulations accounting for the texture of the formation rock and layers of varying conductivity around one or more perforations. The boundary conditions incorporate a pre-defined injection or production flow schedule where a known injection or production rate or pressure response is applied at the grid block corresponding to the perforating tunnel entrance.

The goal of a typical numerical realization is to simulate the pressure response transmitted along the grid, which is sensitive to the 'texture' of the rock. Three different textures have been created: homogeneous formation, conductive vertical fractures, and a horizontally laminated formation. The results can be applied to analyze and visualize the effectiveness of stimulation methods immediately around the perforation region, particularly through the crushed zone.

A numerical simulation was developed in the same fashion as standard reservoir simulators, but with the intent of evaluating near-perforation flow behavior. Starting from the material balance equation and including typical petrophysics parameters that govern the mass transfer between grid blocks, the resulting partial differential equations are linearized using the Newton-Raphson method and solved using the IMPES method. Fluid mechanics analysis such as mass flux and assessment of the flow regime, is done by using conventional porous medium transport relationships.

1. Introduction

Reservoir numerical models have been developed (Williamson and Chappelear, 1981) to simulate the response of an entire field to predict, plan and design the response of well production and/or injection over time, by applying the mass balance equation and related equations (Ertekin, Abou-Kassem and King 2001). For reservoir numerical simulation, a large-scale grid –in the range of miles or km- is normally made, each grid block representing the smallest mathematical unit at which fluid interactions are computed.

The concept for large scale reservoir simulation has been utilized for the development of the smaller scale perforating simulator in this paper - in the range of inches - in order to characterize the response of pressure driving force within a grid block that represents the rock surrounding a wellbore.

In **Fig 1a**, a schematic of the geometry of a perforation tunnel is described, and **Fig 1b** is an actual image of a perforation in a test rock under laboratory conditions (Bakker, et al. 2003). The casing is a mechanical barrier with zero permeability. The perforation tunnel is considered to have a large permeability and porosity and is partially full of debris (disaggregated rock); accordingly, the tunnel cannot be considered as hollow cylinder. The crushed zone is a layer that can extend between 0.25” to 1” beyond the tunnel diameter, the mechanical and fluid properties of the crushed zone have been studied given the importance it has on the production performance of a well. The most critical parameters of the crushed zone are the permeability, porosity and water saturation (Jamiolahmady, et al. 2006), where the values after perforation can be reduced up to 20-30% of the original rock properties, prior to perforation. For purposes of the current simulator, the default value is 30%; however, these numbers can be modified at the user’s discretion. The reservoir grid is the mathematical representation for each individual block in the system; mass transfer (two-phase oil-water) caused by the pressure differential occurs across the grid block boundaries. The driving force is the pressure or flow rate applied at the entrance of the tunnel.

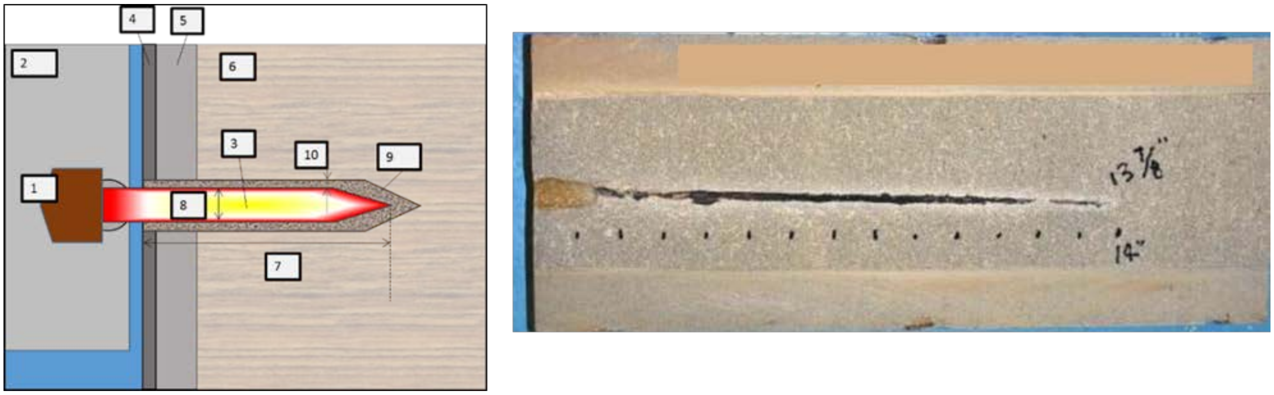

Figure 1a. *Schematics of the perforating geometry: 1. Perforating Charge, 2. Perforating Gun, 3. Perforation jet, 4. Casing, 5. Cement,6. Reservoir rock, 7. Perforation tunnel length, 8. Entrance Hole Diameter, 9. Crushed zone, 10. Crushed Zone Thickness.* ***Figure 1b*** *Image of a perforated core, the tunnel and the damaged zone are clearly visible (Grove, et al. 2012)*

2. Formation and perforation simulation

2.1 The Grid Block. The grid can be predetermined for different grid block configurations in order to simulate features in the formation, such as vertical fractures, horizontal laminations, at either high or low conductivity. Depending on the computation resources available, the number of grid blocks can be increased, however the processing time increases considerably. For the work in this article a grid of 70x70 blocks in cartesian coordinates is used as a framework. **Fig 2** is an example of the simulated grid block. Different values of rock properties (such as porosity and permeability) are assigned on a block-by-block basis.

2.2 The perforation. The guidelines for perforating services in the oilfield industry are defined in the recommended practice API 19B, issued by the American Petroleum Institute (API, 2017). For certain completion types, the most important parameters for evaluating the performance of a shaped charge are the penetration depth and the entrance hole diameter. A sub-code was written in order to build the tunnel according to properties described by (Bolchover and Walton 2006), where the tunnel is not considered as a hollow cylinder, but porous media with high permeability.

2.3 The crushed zone. An important feature is the crushed zone surrounding the perforation tunnel. The simulator has the capability of defining the crushed zone thickness and its petrophysical properties such as porosity and permeability, as a fraction of the original rock conditions.

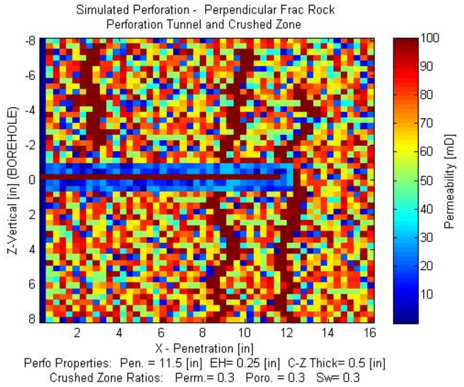

Figure 2 *Numerical simulator grid representing the rock and the perforation tunnel. Dimensions are as per typical API 2" Deep penetration charge. Rock properties (such as permeability) are assigned to each grid block. Perforation Tunnel (Dark Red Section) and Crushed Zone (Dark blue section) are shown. In this illustration the dark red channels are high permeability grid cells, simulating a high conductivity set of fractures.*

3. Mass balance equation and generalized flow equation

The mathematical and physics core of the numerical simulator is the mass balance equation.

Assumptions:

- All processes are isothermal
- Fluids are incompressible and non-reactive.
- No gravity effects on fluid segregation
- Perforation tunnel is considered as high-permeability packed bed with spherical particles.
- Crushed zone permeability and porosity are reduced by a fraction of original values.

A 3D grid cell defined in a cartesian coordinate system is the control volume element through which fluid movement is quantified. This individual block also has specific physical properties as described in **Fig 3.**

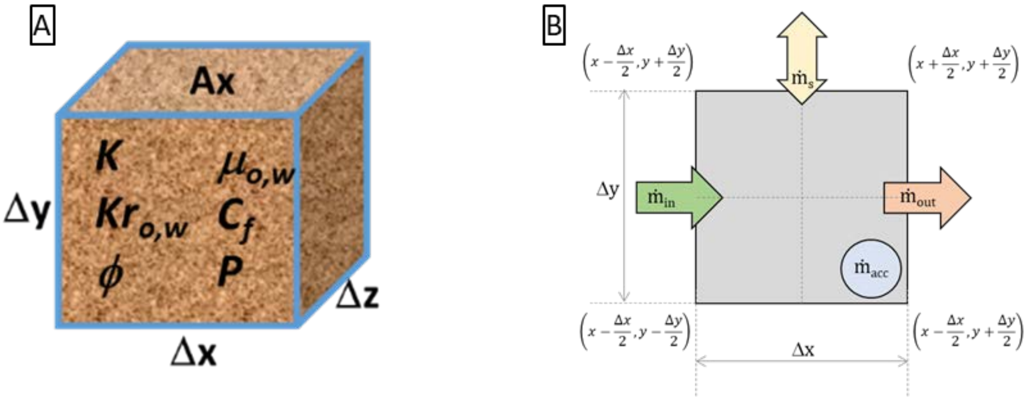

Figure 3- A) *Petrophysical properties of a grid cell.* ***B)*** *Description of mass balance over the control volume*

The components of the mass transfer between blocks are: flow in, flow out, accumulation and production.

$$(m_i - m_o) + m_s = m_a \;, \ldots\ldots\ldots\ldots\ldots\ldots\ldots\ldots\ldots\ldots\ldots\ldots\ldots..(1)$$

Flow in and flow out is the mass transfer that occurs between adjacent cells, due to the pressure differential present at every time step. The sink or source mass flow is the amount of mass that is added or removed from the system; in large scale reservoir simulations the sink or source point represents the production or injection wells, but for the case of the perforation simulator, the sink and source will be the fluid that is injected or produced at the grid cell corresponding to the entrance hole in the perforation tunnel. Finally, accumulation is the amount of mass that is stored in the block during that specific time step.

The purpose of the simulator is to quantify the effect of the pressure or flow rate variation exerted at the entrance hole and calculating how it will spread along the grid over a definite time, by considering the petrophysical properties of the simulated rock.

The mass balance equation is written in terms of flow rate, by defining the mass flow rate m as the product of volumetric flow rate q and density ρ. The mass balance equation in two dimensions over a definite interval Δt, can be expressed as **Eq 2**.

$$\left[(m_{io})_{x-\frac{\Delta x}{2}}\Delta t + (m_{io})_{y-\frac{\Delta y}{2}}\Delta t\right] - \left[(m_{io})_{x+\frac{\Delta x}{2}}\Delta t + (m_{io})_{y+\frac{\Delta y}{2}}\Delta t\right] + m_s\Delta t = (\phi\rho\Delta x\Delta y)_{t+\Delta t} - (\phi\rho\Delta x\Delta y)_t \text{ , ...(2)}$$

Referring to **Fig 3-B**, the first two terms in **Eq 2** represent the amount of mass that flows in (**m_{in}**) and out (**m_{out}**) of the control volume. For the x-axis, such in and out flow occur at walls located at x-Δx/2 and x+Δx/2 respectively. A similar analysis can be done for y and z axis. The term $m_s\Delta t$ refers to the mass that is extracted from (sink) or added to (source) the system, and the terms on the right-hand side are the accumulated mass (***m_a***) within the control volume over the period Δt.

Applying the concept of differentiation when the control volume dimension and time increment are taken to limit approaching zero, the material balance results in PDE:

$$-\frac{\partial}{\partial x}(\rho u_x A_x)\Delta_x - \frac{\partial}{\partial y}(\rho u_y A_y)\Delta_y + \frac{m_s}{\alpha_c} = \frac{V_b}{\alpha_c}\frac{\partial}{\partial x}(\phi\rho) \text{ , ...(3)}$$

By taking definitions of Darcy law for flow through porous media, the superficial velocity in i direction can be expressed as"

$$u_i = -\beta_c \frac{k_i}{\mu}\frac{\partial\varphi}{\partial i} \text{ ... ...(4)}$$

Combining **Eq 3** and **Eq 4**, it is obtained the 2D cartesian governing equation (**Eq 5**) for reservoir engineering applications:

$$\frac{\partial}{\partial x}\left[\beta_c K_x A_x \frac{K_{rl}}{\mu_l B_l}\left(\frac{\partial P_l}{\partial x}\right)\right]\Delta_x + \frac{\partial}{\partial y}\left[\beta_c K_y A_y \frac{K_{rl}}{\mu_l B_l}\left(\frac{\partial P_l}{\partial y}\right)\right]\Delta_y = \frac{V_b}{\alpha_c}\frac{\partial}{\partial t}\left(\frac{\phi\, S_l}{B_l}\right) - q_{lc}, \text{ ... ...(5)}$$

Where l indicates the phase (oil or water), K_x is the arithmetic average of permeability between adjacent grid cells, A_x is the area of flux, Kr_l is the relative permeability, μ_l is the fluid viscosity, B_l is the formation volume factor, β_c is the conversion factor from metric to oilfield units, and q_{lc} is the fluid produced or injected in the system (sink or source). The petrophysical and fluid parameters are integrated in the transmissibility term, as described in appendix 2.

4. Numerical method solutions

The partial differential equation **Eq 5** is solved by using the numerical method of Newton Raphson, and implicit explicit -IMPES- technique (Anderson, 2013). Full details of the mathematical derivation of the code for the simulator are provided in Appendix 2.

4.1 Boundary Conditions The external border of the grid must be considered as open flow or Constant-Pressure boundary. To model that boundary condition, the original grid size *(Nx,Ny)* is imposed over a 'ghost' matrix of size *(Nx+1,Ny+1)* as described in (Ertekin, Abou-Kassem and King 2001) . The fictitious matrix is a set of external sink/source gridblocks at constant formation pressure that compensates for fluid transfer within the grid. In other words, it doesn't restrict the flow transfer as opposed to No-Flow boundaries. The fictitious matrix is the numerical representation of an infinite reservoir at a given formation pressure. The x=0 line corresponding to well completion (cemented casing) the permeability is set to 0 mD.

4.2 Driving force The driving force on the system is the mechanism that will produce the movement of fluid in the system. It will be applied at the grid cell corresponding to the entrance hole of the perforation tunnel, and the simulator will calculate how the driving force will spread along the grid, based on the calculation of mass transfer between adjacent cells at every time step. The driving force in the simulator can be given in two different ways according to normal practices in the oilfield: 1) Flow Rate Scheme or 2) Pressure Transient. Both driving forces can be applied either in production (sink) or injection (source) modes, and they can be adjusted to constant or variable pumping schedules. In production or stimulation jobs the pumping schedules are designed at different rates during minutes or hours, whereas in the case of perforations the fluid dynamic transient occurs within a few seconds after the perforation guns are detonated; in this case the time steps are in the order of seconds.

4.3 Solution for different driving force schemes. The approach for the simulator is to solve the partial differential equations for mass balance. Initial conditions are set for boundary and system reservoir conditions where the initial pressure on each cell of the grid P_i^n is known.

For the case of driving force scheme 1, a defined Flow Rate Q is applied at the sink/source grid cell (the tunnel entrance hole). The key fact for the solution is that the Flow Rate $Q_{ss}{}^n$ is *known* at every time $n=1 \longrightarrow t$ of the process, then the system iterates on the mass balance equations to find the *new* set of pressure values P_i^{n+1} for the system at next time step $t+\Delta t$.

For the case of scheme 2 with the driving force as Pressure Transient, the pressure $P_{ss}{}^n$ applied in the sink/source grid cell is *known* for every time $n=1 \longrightarrow t$, but the flow rate $Q_{ss}{}^n$ is unknown. The matrices in the numerical code are arranged in a certain way to accommodate the unknown values and obtain the next step values for pressure in the rest of the grid P_i^{n+1}, and flow rate in the sink/source grid cell $Q_{ss}{}^{n+1}$.

Fig 4 is an illustration of the two different driving force schemes on a linear grid, at initial conditions n and after first iteration $n+1$. The known values are highlighted in green and the unknowns in red.

The iteration in the simulator is repeated to a number of acceptable time steps, depending on the nature of the work to be simulated. The user must ensure processing convergence and numerical stability is achieved to validate the results. See Appendix 3 for a detailed analysis.

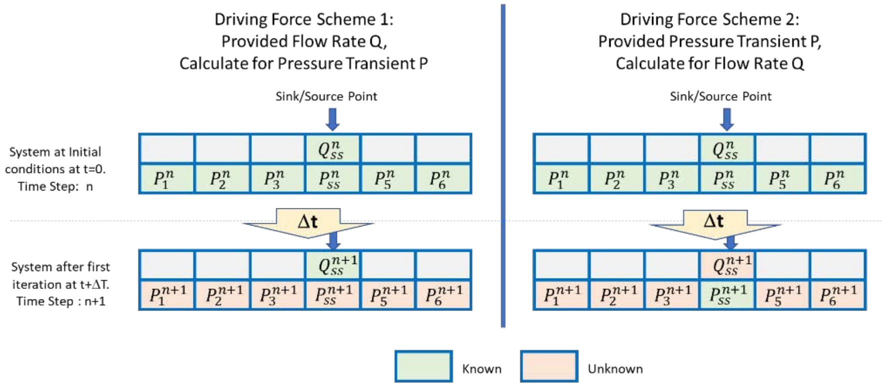

Figure 4 *– Illustration in a 1-Dimension grid block at the current time step* ***n*** *and the calculated next step values at* ***n+1****. The known values are highlighted in green and the unknowns in red. The driving force is applied at the sink-source cell.*

5. Fluid Mechanics at the perforation tunnel

Fluid mechanics calculations in the perforation tunnel were done using equations developed for mass transfer in porous media based on Ergun equation (Ergun 1952), with the application of pipe packed with spherical beads in the laminar to turbulent transition region (Jamiolahmady, et al. 2006). The first term of **Eq 6** is the Carman-Kozeny equation, which is applicable to laminar flow, and the second term is the correction for inertial effects at higher flow rates (Akgiray and Saatçı 2001), (Bird, Stewart, W.E, and Lightfoot, E.N. 2009).

$$\Delta P = \frac{150\mu L}{d_p^2}\frac{(1-\phi)^2}{\phi^3}v_s + \frac{1.75L\rho}{d_p}\frac{(1-\phi)}{\phi^3}v_s|v_s| \dots\dots\dots\dots.\dots(6)$$

Where ΔP is the differential pressure across grid cells in within the perforation tunnel, μ is the viscosity of the fluid, L is the length of the grid cell, d_p is the effective diameter of the particle, ϕ is the porosity of the tunnel, and V_s is the velocity of the fluid.. Note that units in **Eq 6** are in the metric system as found in the literature. Conversion to field units is considered in the code.

The effective porosity inside the perforation tunnel on this particular setup is calculated as described by Nao, 2008 using the relationship $\phi = 0.151/(D/d_p - 1) + 0.360$, applicable for $D/d_p > 2.033$. It is assumed that the debris filling the perforation tunnel is spherical shape, with a diameter of 1/10th of the tunnel diameter. ($D/d=10.$)

The instantaneous fluid volume produced/injected through the perforation is calculated by considering the flow rate *at the grid cell corresponding to the tunnel entrance*, over the defined time step Δt, by using $V = \Delta t * Q$. Packed bed fluid velocity is calculated by solving the Ergun equation for velocity term v_s. The *Eq 15* is a quadratic polynomial and the roots are the numerical solution for velocity v_s.

Finally, the Reynolds number is calculated using the equation for packed bed -**Eq 7-** as described by Dwivedi 1977. The simulator calculates the reynolds number at every grid cell, as a function of fluid velocity.

$$Re = \frac{v\, d_{debris}\, \rho_f}{\mu\, (\phi_{tunnel})}\ , \dots\dots\dots\dots\dots\dots\dots\dots\dots\dots\dots\dots\dots\dots\dots (7)$$

The simulator is able to calculate the flow regime in the system, identifying those areas where there is turbulent, laminar or transient flow.

6. Results

Two different scenarios were built for analyzing the flow performance under different grid conditions: 1) Homogeneous formation **Fig 5-A** and 2) Horizontally laminated formation **Fig 5-B**. A 20in block was simulated with a perforation tunnel typical of a conventional deep penetrating 2” charge, consisting of penetration of 11.5 in and Entrance Hole 0.25in. The grid block is built in two-dimensional cartesian coordinates since the main interest is to describe the flow behavior through the grains of rock surrounding the borehole. A cartesian 2-D grid cell (compared to a cylindrical framework) allows a more accurate mathematical model of the rock grains and petrophysical properties. Additionally, formation features like conductive or sealed fractures can be modeled -and results interpreted- with higher detail, and easier coding implementation in the numerical model.

Other simulators (Arton, 2017, Karimi-Fard, 2012) use cylindrical coordinates for mathematical convenience of flow paths, although the representation for grain sizes will not be representative at larger distances from the axial line, unless refined grid cells are used along the grid block,

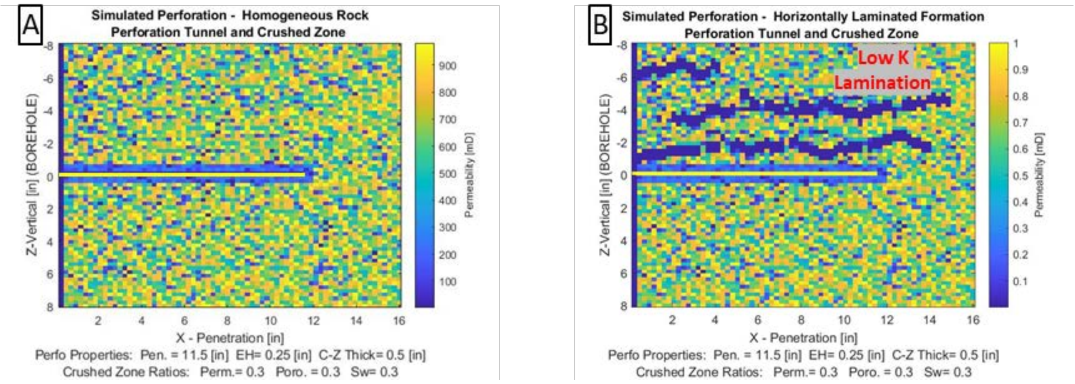

Figure 5 *Simulated grid blocks with different textures, perforations and crushed zones: A) Homogeneous, B) Horizontally laminated.*

6.1 Driving force Scheme 1: Given Flow Rate Q, Calculating for Pressure P. For the first two scenarios the well is fed by a constant flow rate Q = 7 BPM. The pressure mapping demonstrates that the pressure distribution is sensitive to rock texture, given that the permeability and porosity of the grains are represented on the initial grid.

For scenario 1, Injection in homogeneous formation from 0 to 100 sec, the results of the simulator are displayed in a 2D pressure mapping. **Fig 6** is the pressure distribution at t = 100 s. (Detailed elapsed time figures and description are provided in Appendix 1, **Fig A1-2**, for a horizontally laminated formation). It is observed that the pressure distribution that started at the entrance hole, is uniformly distributed along the perforation tunnel where there is high permeability. The fluid flows across the damaged zone and creates a considerably high-pressure region across the crushed zone. Then the fluid is dispersed into the formation. It is important to observe that the simulator results are sensitive to those grid cells (rock grains) with high or low permeability.

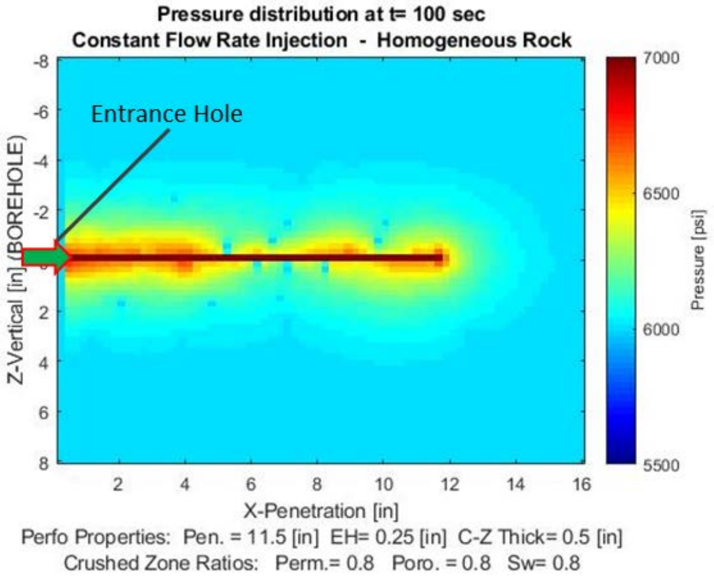

Figure 6 *Pressure distribution for a homogeneous rock at t=100s. The green arrow represents the fluid inflow in the system as is being injected at constant flow rate Q=7 bpm, applied at the entrance hole of the tunnel -the sink/source cell-.*

The evolution of the pressure in the line along different cross sections on the simulated grid block is displayed in **Fig 7**. The analyzed pressure distribution is the final iteration at t=100 sec (**Fig 7-A**)

In **Fig 7-B** each curve represents the pressure profile as a horizontal cross-section at the perforation tunnel, for different times from t = 0 to t = 100 sec showing time increments of 20 seconds. At t = 0 the system is at initial conditions, with a uniform and constant reservoir pressure of 6000 psi; the initial pressure profile at t = 0 sec remains flat at 6000 psi, since no fluid has entered in the system. During the first-time step at t = 20 sec, the fluid injected at constant rate acts as the driving force at the entrance hole. The mass inflow produces a pressure differential that is transmitted between adjacent cells and is distributed uniformly along the perforation tunnel, which is observed by a pressure gradient starting at 7500 psi at the tunnel entrance, decreasing to ~6700 at the end of the tunnel (x = 11.5 in). After the tip of the tunnel, the pressure decreases gradually until it reaches again 6000 psi at 16in, which is where the boundary condition of constant pressure is observed. The same profile is gradually increasing at every time increment up to a maximum at t = 100sec.

A similar analysis is done at the x-line of the crushed zone in **Fig 7-C**. The pressure at the crushed zone is smaller compared to that of the perforation tunnel as the fluid finds more resistance to flow into the grid cells of lower permeability in the rock. The spikes on the curve represent the variations of the randomly assigned permeabilities at each grid cell: the pressure profile will show low pressure in the location of low permeability grains, honoring the flow restrictions given by transmissibility between adjacent grid cells.

In **Fig 7-D** is displayed a cross-section pressure profile in the Z direction, in the middle of the perforation tunnel. At the upper and lower ends, the pressure corresponds to formation pressure P=6000 psi. When the curve approaches the crushed zone, the pressure increases gradually to a maximum inside the perforation tunnel in the centerline.

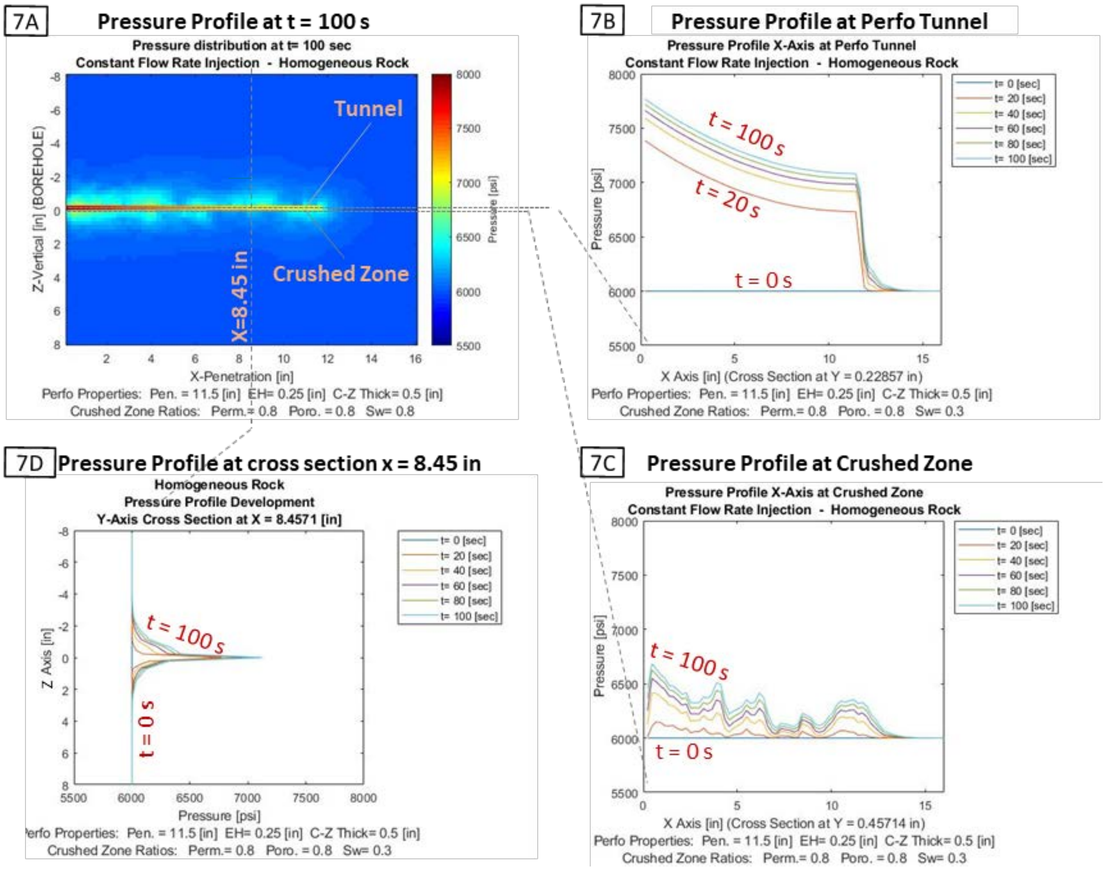

***Figure** 7 Pressure profile evolution for different times, at different cross-sections within the matrix. A) Grid block with perforation, B) X-Section at the tunnel, C) X-Profile at crushed zone, and D) Z-Section at x=8.64in.*

For scenario 2) Constant flow rate injection in horizontally laminated formation, the pressure distribution and pressure plot analysis follow the permeability restrictions as determined in the initial grid, as displayed in **Fig 8-A.** When the perforation occurs within a vicinity of low permeability layer, the flow is limited and the mass transfer only occurs at the higher permeability region where favorable conditions exist.

The pressure profiles at vertical cross section are plotted in **Fig 8-B**. Since the perforation tunnel is directly in contact with the low permeability layer, the upper section of the pressure profile is not developed, meaning that the fluid cannot flow through the formation. The pressure profile at different time steps from 0 to 100 sec is only developed in the lower section of the perforation tunnel.

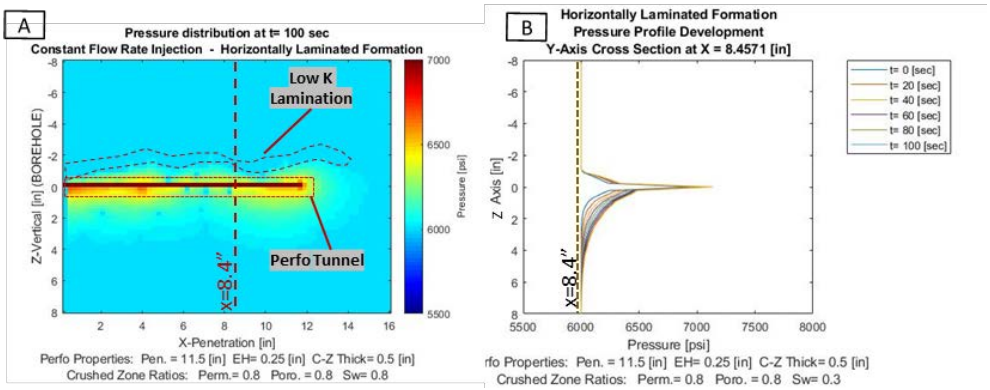

Figure 8 *Pressure distribution for scenario '2) Constant flow rate injection in horizontally laminated formation'.* ***Fig 8-A*** *is the two-dimension pressure distribution, highlighting the location of the low permeability layer above the perforation tunnel: the pressure distribution is limited by the simulated barrier.* ***Fig 8-B*** *Pressure profiles of a vertical cross-section at x=8.4" in the tunnel. Showing the development from 0 to 100 sec. The pressure gradient is observed only in the lower region of the grid block.*

An important result to analyze is to compare the pressure profiles between High-Damage crushed versus Low-Damage crushed zone. The High-Damaged crushed zone is mathematically defined by reducing the permeability and porosity of the grid cells surrounding the perforation tunnel to a factor of 0.3 of original rock conditions, prior to the perforation. The reduction in permeability is known as K_c/K. The reduction in porosity (same factor of 0.3) is due to the accumulated pulverized debris in the tunnel surface and the compression of the crushed zone during the perforation event. The Low-Damage crushed zone is obtained by applying a factor of 0.8 of original rock properties for permeability and porosity. All other parameters remain unchanged. The crushed zone improvement from High to Low damage could be the effect of an acidizing or stimulation job (Bartko, 2007; Oeth, 2013) or dynamic underbalanced perforating where some of the damage is removed. In this example, the damaged zone factor of 0.3 and 0.8 are assigned manually according to values found in literature either by estimating the flow conductivity (Li, 2015), or the core flow efficiency (Grove, 2011). The coefficient could be modified at the users discretion.

The pressure profiles in **Fig 9** correspond to constant injection flow rate of in a horizontally laminated formation, at the cross-section of the damaged zone. **Fig 9-A** shows the resulting pressure profiles for high-damage zone factor 0.3, obtaining a maximum pressure of ~9,500 psi; **Fig 9-B** shows results for a low-damage zone factor of 0.8, achieving a maximum pressure of ~7,300 psi. Both results are plotted on a similar pressure scale. As expected, the pressure profiles for the low-damage scenario are reduced considerably, meaning that the skin of the perforation tunnel has effectively been improved. This is a useful output of the simulator to measure productivity and injectivity efficiency.

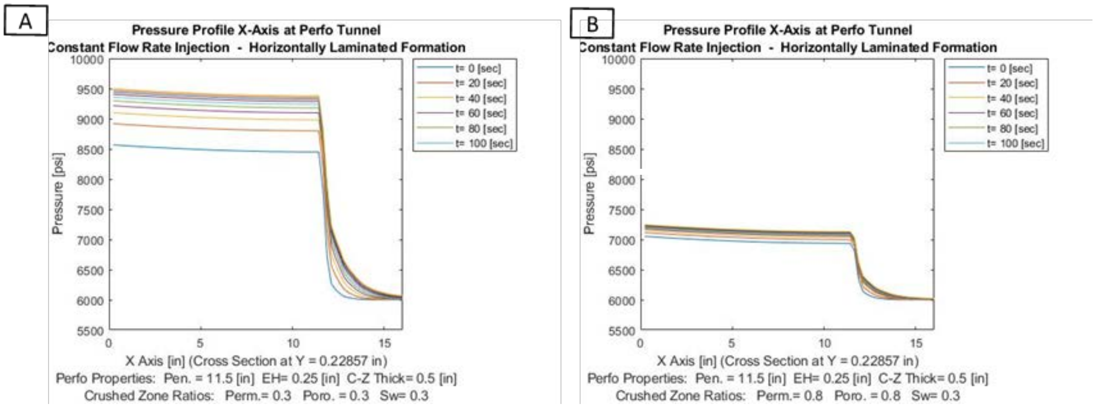

Figure 9 *Pressure grid and perforation simulation for A) High-Damage crushed zone and B) Low-Damage crushed zone*

6.2 Driving force Scheme 2: Given Pressure Transient P, Calculating for Flow Rate Q - Dynamic Underbalance Perforation Simulation

Dynamics underbalanced (DUB) perforating is perhaps the most relevant example in terms of accuracy and precision of the model, given that the pressure transient occurs in fractions of a second. During a dynamic underbalanced perforation, the pressure transient is designed and measured to manipulate the pressure in the borehole at the entrance of the perforation tunnels, aiming to produce a negative pressure that will in turn create a sudden flow movement to remove the debris in the perforation tunnel, immediately after the tunnel is created (Heiland, et al. 2009)

The DUB pressure transient is used as the driving force for the simulator, and is represented by a pressure-time curve, approximated from literature (Bakker 2003). **Fig 10** represents an idealized pressure-time profile, enabling the user to analyze the performance of the simulator at every time and its respective pressure transient variation. For real case scenarios, the dynamic underbalanced pressure-time curves are plotted from measured data downhole, showing a more ‘irregular’ profile.

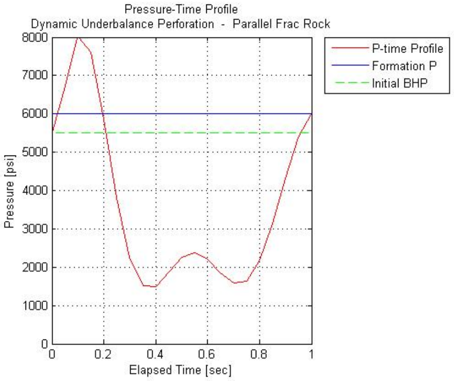

Figure 10 Pressure transient for dynamic underbalanced perforation. The user can define the borehole and reservoir pressure at initial conditions

The images in **Fig 11** are the output of the simulator, consisting of 2D Pressure distributions and fluid velocity vector field at t=0.4 sec, where the fluid is being withdrawn from the tunnel. The vector field replicates the flow lines around the perforation tunnel as suggested by (Grove, Harvey and Zhan 2011), confirming that the simulator offers a mathematical framework to analyze the fluid dynamics at the perforation tunnel.

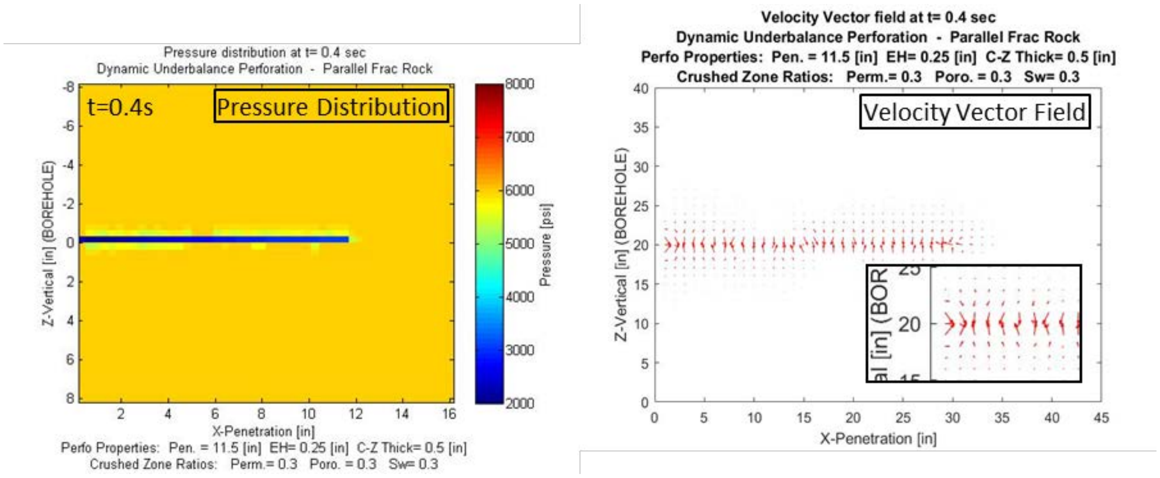

Figure 11. *Time development for Pressure distribution, Surface velocity field for Dynamic Underbalance Perforation at t=0.4 s. Images of the full sequence from t=0 s to t=1.0 s are displayed in Appendix 1, Fig A1-4.*

In the appendix **Fig A1-4** is displayed a sequence of images obtained from the simulator from t=0 to t=1 sec, to visualize the complete sequence of the pressure transient. It is observed that the simulator accurately describes the pressure distribution initiated at the entrance of the perforation tunnel. The importance of characterizing the velocity vector field rely on further applications of the simulator involving the fluid mechanics and effective stresses around suspended particles during underbalanced perforation. For instance, to measure the effectiveness of solids removal from within the tunnel and crushed zone. At t=0 s, there is a small negative spike corresponding to the initial wellbore underbalanced of -500 psi; in the velocity vector field there is a small perturbance by the small pressure differential. From t=0 to t = 0.2 s there is a sudden overbalance caused by the gun detonation, as observed on the pressure distribution. The positive pulse from the detonation at t = 0 s creates an 'outward' flow out of the tunnel.

At t = 0.2 s, there is a transition in the velocity vector field, where a 'front wave' is visualized by the arrow in line with the perforation tunnel and indicating that the fluid is surged out of the perforation into the borehole. After t = 0.2 s, the effect of the dynamic underbalanced perforation system is observed at the perforation tunnel, transmitting the pressure transient along the tunnel and across the crushed zone into the formation, following the pressure variations occurring in the underbalanced period.

An important observation is the sensitivity of the simulator to oscillations in the pressure transient, by comparing the direction of the velocity field at the entrance of the tunnel at t=0.6 and 0.8 s, as shown in **Fig 12** (a close-up from the overall velocity field). At t = 0.6s, the arrows indicate an instantaneous inwards flow (fluid transferred from the tunnel entrance onto the formation), but at t = 0.8s, the arrow at the tunnel entrance is facing the opposite direction, which indicates a dominant outward flow as effect of the DUB surge.

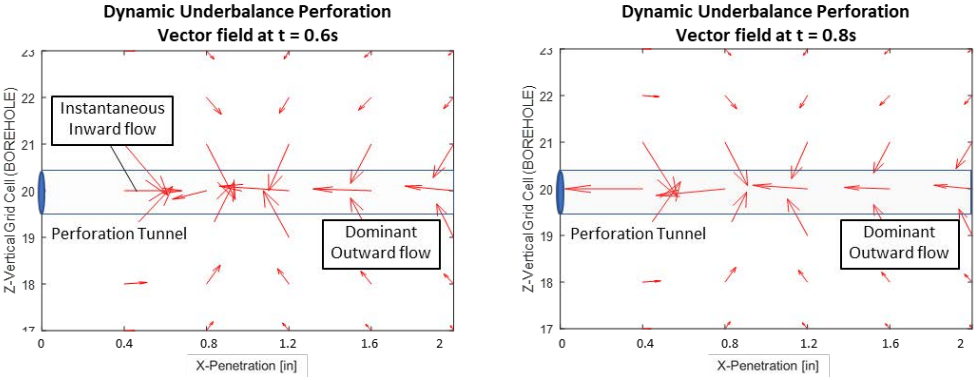

Figure 12 *Close up of the arrow field at t=0.6 during DUB perforation described in fig 10. Even though the dominant flow direction created by the surge is outwards, there are local changes in the direction of the fluid caused by the oscillating pressure transient at the tunnel entrance, producing an instantaneous inward flow. The simulator is sensitive enough to visualize these fluctuations in the driving force. At t=0.8s, the DUB surge flow is outwards, providing the fluid dynamic conditions to clean up the debris and remove the damaged zone in the tunnel.*

Once the underbalanced energy is depleted after t = 0.8 s, the pressure stabilizes again back to formation pressure. A positive pressure is observed in the tunnel and surrounding grid cells. The pressure transient finishes at t=1.0 s, with the velocity vector field showing that the fluid is injected into the formation.

Another example of visualizing the effectiveness of the "Given P Calculate Q" mode of the code is to simulate the production of fluid at constant pressure – or any other pumping schedule. The driving force in this example is a continuous drawdown of 1000 psi (flowing pressure 5000 psi) applied at the entrance of the perforation tunnel in a homogeneous rock with a formation pressure of 6000 psi. Two scenarios are presented with different damage conditions at the crushed zone; High Damage Conditions (Damage Factor 0.3) vs Low Damage Conditions (Damage Factor 0.8) over a time period from 0 to 100 sec. From the two-dimension pressure distributions in **Fig 13-A**, it is observed that the high damage case presents a larger area affected by pressure differential from the tunnel towards the reservoir, showing a larger area of pressure 'disturbance' compared to the case of low damage in **Fig 13-B.**

The distance-pressure plot in **Fig 13-C** shows the penetration in the horizontal axis and the drawdown pressure in the vertical axis at the crushed zone and in the perforation tunnel. The pressure profile at the tunnel is a decaying curve, indicating that the system follows the boundary condition of 1000 psi drawdown at the entrance, followed by a steady decrease along the tunnel until the distance of maximum penetration (x=11.5") to a value of 180psi, as the pressure is transmitted between the 'homogeneous' grid cells conforming the tunnel, then dropping to reservoir pressure (zero drawdown) into the reservoir. The pressure profile for the crushed zone, in the other hand, shows a larger variation as a response to the petrophysical properties assigned to the surrounding grid cells (the 'rock grains'). Those spots with zero drawdown are caused by Low permeability grains (LKG in the plot). The pressure profile shows a maximum pressure of 580 psi near the entrance of the tunnel, decreasing to ~60 psi at the tip of the tunnel (maximum penetration x=11.5"), and dropping to zero drawdown into the reservoir.

The x-penetration vs pressure plot for the case of low damage **Fig 13-D** indicate that the pressure profile in the tunnel decreases from 1000 psi at the entrance, to nearly zero at the tip of the tunnel. The profile at the crushed zone level starts at 400 psi, decreasing to zero at around 7 in from the entrance. The later pressure profile has a zone of mild variations as an effect of the petrophysical properties of the grid cells. The lower drawdown compared to the high damage case is an indication that the fluid will flow with less restrictions into the tunnel, having reduced the perforation skin (for example as a result of a well treatment). The pressure distribution along the tunnel is consistent with the stress finite method analysis as described in JRC, 2011, which shows that the higher concentration of the local maximum principal stress occurs near the entrance of the tunnel.

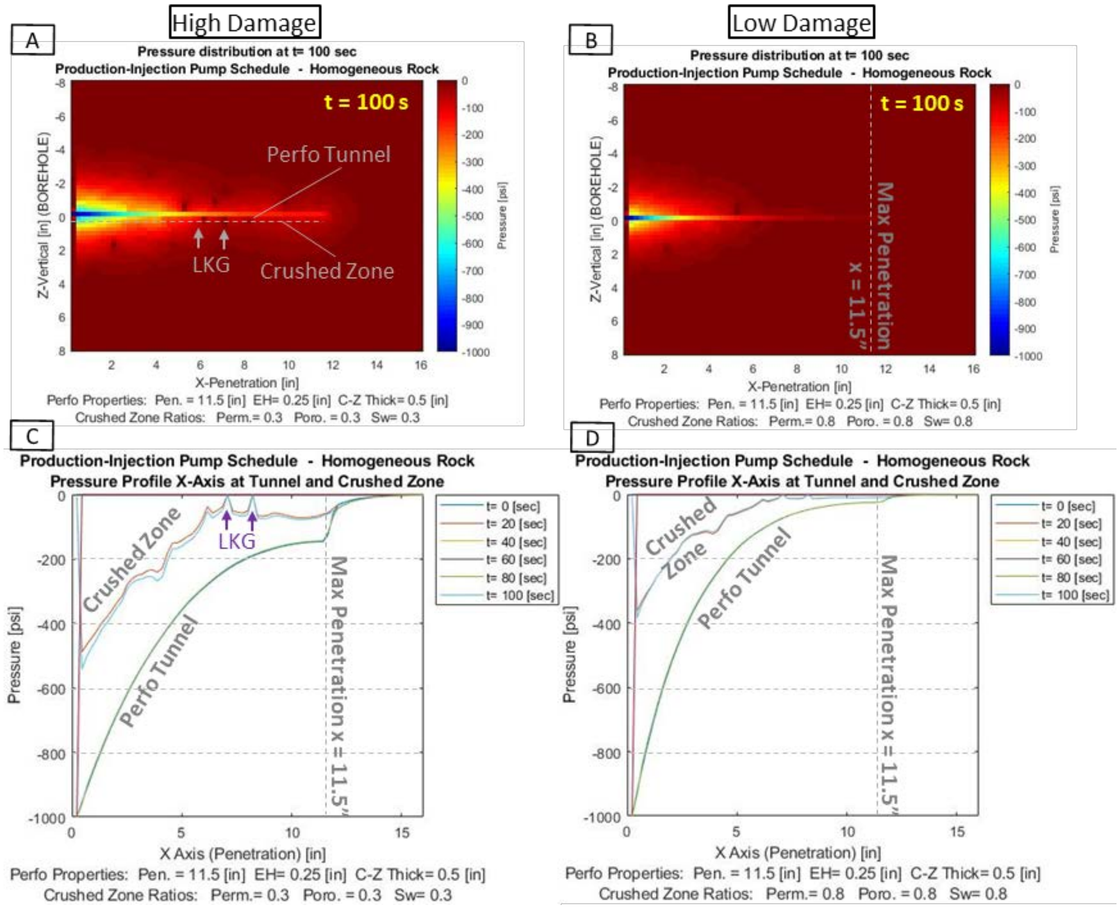

***Figure 13** Example of the "Given P calculate Q" mode of the simulator, by producing at a constant drawdown of 1000 psi over two scenarios of high damage vs low damage around perforation tunnel. On the left side, **Fig 13-A** is the pressure distribution along the 2D grid for the 'high damage' scenario (Crushed zone ratio = 0.3). **Fig 13-C** is the penetration vs pressure plots at the crushed zone and at the perforation tunnel. The pressure developed at the crushed zone along the tunnel, showing the boundary condition of pressure drawdown = -1000 psi at the entrance of the tunnel, and decreasing until the tip of the tunnel (x=11.5"), then dropping to zero (achieving reservoir pressure) at the border of the grid block (x=16 in). The system is reaching steady-state*

conditions at from early time t=20 s. ***Figs 13-B*** *and* ***13-D*** *shows the pressure distribution and profile development for the 'low damage' scenario (Crushed zone ratio = 0.8).*

7. Conclusions

The proposed fluid mechanics perforation simulator in the near borehole region is a powerful tool to visualize and evaluate the pressure transient at the perforation tunnel, crushed zone, and nearby region. Multiple variables can be modified at users' discretion to analyze the response of a pressure transient or pumping schedule on both the rock and reservoir fluids. Perforation parameters, rock texture and reservoir fluid characteristics can be changed to analyze different perspectives of the interaction of the pressure and fluid responses that can be used for typical well interventions.

The two-dimensional pressure distribution and field velocity provide more intuitive displays to understand the implications of having a damaged zone, and the benefits of designing effective treatments to improve the flowing conditions in the perforation tunnel. The distance-pressure plot provides a pressure profile along the tunnel that enables visualization of the behavior of the fluid with respect to the simulated petrophysical properties in the grid block.

The simulator provides a solid mathematical framework that needs to be validated and adjusted with respect to experimental results. From the numerical point of view, the user must perform convergence and stability analysis to ensure that the results are consistent. The simulator is flexible enough to process a wide range of variables.

Given that the numerical code is developed from basic material balance equations, further applications can be implemented for particular cases: Fluid dynamics analysis to estimate the drag forces and predict the effectiveness of the cleanup of the perforation tunnel; analyzing the effect of reactive fluids during acid stimulations; and convective and diffusive mass transport phenomena for non-Darcy fluid-rock interactions.

It is understood that the initial development of the mathematical solution is a single plane, and it is not a realistic representation of the real downhole scenario. A full model will be implemented over a 3D grid block, where different scenarios can be built; for instance, to analyze the interaction between 2 perforation tunnels, and to have a better approach to fluid velocity and fluid volume calculation.

8. Nomenclature

a_c	Accumulation constant
$A_{x,y,z}$	Area of flow of Grid Cell [m^2]
B_l	Formation Volume Factor, *l=oil or water* [no units]
β_c	Conversion Factor from Metric to Oilfield Units
c_f	Rock Compression [1/psi]
d_p	Effective diameter of particles in sphere packed bed [in]
ρ	Fluid Density [kg/m^3]
$\Delta x,y,z$	Grid Cell dimensión in x,y, and z direction [m]
ΔP	Pressure differential across grid cells [psi]
K	Permeability [mD]
K_{rl}	Relative Permeability, *l=oil or water* [mD]
L	Length of grid cell [in]
$\dot{m}_{in/out}$	Mass Flow Rate: Fluid transferred between adjacent cells [kg/s]

$\dot{m}_s$	Mass Flow Rate: Sink or source, Fluid added/removed from the system [kg/s]
$\dot{m}_{acc}$	Mass Flow Rate: Fluid accumulated in the grid cell [kg/s]
μ_l	Viscosity, *l=oil or water* [Pa/s]
$P_{i,j}$	Pressure at location *i, j* [psi]
P^{n+1}	Pressure at current time step [n] [psi]
P^{n+1}	Pressure at next time step [n+1] [psi]
Q	Volumetric Flow rate [BPM]
Φ	Porosity [%]
S_w	Water Saturation [%]
S_o	Oil Saturation [%]
$u_{x,y}$	Fluid Velocity [m/s]
V_b	Bulk Volume [m^3]
v_s	Packed bed superficial velocity [ft/s]
w	mass flow rate [kg/s]

9. References

Akgiray, Ö., & Saatçı, A. M. (2001). A new look at filter backwash hydraulics. *Water Science and Technology: Water Supply*, *1*(2), 65–72. https://doi.org/10.2166/ws.2001.0022

Anderson, D., Tannehill, J. C., & Pletcher, R. H. (2016). Computational fluid mechanics and heat transfer, Third edition. *Series in Computational and physical process in mechanics and thermal sciences* (Third edit, pp. 1–740). CRC Press. ISBN: 9781466578302

API. (2019). API (American Petroleum Institute) Standards. Retrieved May 20, 2019, from API website: https://www.api.org/products-and-services/standards

Bakker Kees Veeken Nederlandse Aardolie Maatschappij, E., Behrmann, L., Milton Gary Stirton, P., Salsman, A., Stutz, L., Underdown ChevronTexaco Houston, D. Thompson, F. (2003). The New Dynamics of Underbalanced Perforating. *Oilfield Review*, *15*(4), 54–67.

Bartko, K. M., Chang, F. F., Behrmann, L. A., & Walton, I. C. (2007). Effective Matrix Acidizing in Carbonate Reservoir - Does Perforating Matter? *SPE Middle East Oil and Gas Show and Conference*. https://doi.org/10.2118/105022-MS

Bird, R. B. Robert B., Stewart, W. E., & Lightfoot, E. N. (2006). Transport phenomena. (2nd ed., p. 928). J. Wiley. ISBN: 9780470115398

Bolchover, P., & Walton, I. C. (2006). Perforation Damage Removal by Underbalance Surge Flow. *SPE International Symposium and Exhibition on Formation Damage Control*. https://doi.org/10.2118/98220-MS

Chang, F. F., Kageson-Loe, N. M., Walton, I. C., Mathisen, A. M., & Svanes, G. S. (2004). Perforating in Overbalance - Is It Really Sinful? *SPE Drilling & Completion*, *19*(03), 173–180. https://doi.org/10.2118/82203-PA

Chang, F. F., Mathisen, A. M., Kågeson-Loe, N., Walton, I. C., Svane, G., Midtbø, R. E, Nedrebø, O. (2005). Recommended Practice for Overbalanced Perforating in Long Horizontal Wells. *SPE European Formation Damage Conference*. https://doi.org/10.2118/94596-MS

Chapra, S. C., & Canale, R. P. (2015). *Numerical methods for engineers* (7th ed.). New York: McGraw-Hill Education. ISBN: 007339792X

Dwivedi, P. N., & Upadhyay, S. N. (1977). Particle-Fluid Mass Transfer in Fixed and Fluidized Beds. *Industrial and Engineering Chemistry Process Design and Development*, *16*(2), 157–165. https://doi.org/10.1021/i260062a001

Ergun, S. (1952). Determination of Geometric Surface Area of Crushed Porous Solids. *Analytical Chemistry*, *24*(2), 388–393. https://doi.org/10.1021/ac60062a033

Ertekin, T., Abou-Kassem, J. H., & King, G. R. (2001). *Basic Applied Reservoir Simulation* (SPE texbook). Richardson, Tex. : Society of Petroleum Engineers. ISBN: 1-55563-089-8

Fand, R. M., & Thinakaran, R. (1990). The Influence of the Wall on Flow Through Pipes Packed With Spheres. *Journal of Fluids Engineering*, *112*(1), 84. https://doi.org/10.1115/1.2909373

Grove, B. M., Harvey, J. P., & Zhan, L. (2011). Perforation Cleanup via Dynamic Underbalance: New Understandings. *SPE European Formation Damage Conference*. https://doi.org/10.2118/143997-MS

Heiland, J. C., Grove, B. M., Harvey, J. P., Walton, I. C., & Martin, A. J. (2009). New fundamental insights into perforation-induced formation damage. *8th European Formation Damage Conference*. https://doi.org/10.2118/122845-MS

Jamiolahmady, M., Danesh, A., Sohrabi, M., & Duncan, D. B. (2006). Flow around a rock perforation surrounded by crushed zone: Experiments vs. theory. *Journal of Petroleum Science and Engineering*, *50*(2), 102–114. https://doi.org/10.1016/J.PETROL.2005.10.004

JRC, (2011). *210 MaxForce-FRAC*. Jet Research Center, https://www.jetresearch.com/content/dam/jrc/Documents/Brochures/MaxFORCE-FRAC-H08708.pdf , accessed 2019-09-19

Karimi-Fard, M., & Durlofsky, L. J. (2012). Accurate resolution of near-well effects in upscaled models using flow-based unstructured local grid refinement. *SPE Journal*, *17*(4), 1084–1095. https://doi.org/10.2118/141675-PA

Li, N., Dai, J., Liu, P., Luo, Z., & Zhao, L. (2015). Experimental study on influencing factors of acid-fracturing effect for carbonate reservoirs. *Petroleum*, *1*(2), 146–153. https://doi.org/10.1016/J.PETLM.2015.06.001

Oeth, C. V., Hill, A. D., Zhu, D., & Sullivan, R. B. (2013). Characterization of small scale heterogeneity to predict acid fracture performance. *Journal of Petroleum Science and Engineering*, *110*, 139–148. https://doi.org/10.1016/J.PETROL.2013.08.001

Okumura, M., Yuki, K., Hashizume, H., & Sagara, A. (2005). Evaluation of Flow Structure in Packed-Bed Tube by Visualization Experiment. *Fusion Science and Technology*, *47*(4), 1089–1093. https://doi.org/10.13182/FST05-A832

Okumura, M., Yuki, K., Hashizume, H., & Sagara, A. (2005). Evaluation of Flow Structure in Packed-Bed Tube by Visualization Experiment. *Fusion Science and Technology*, *47*(4), 1089–1093. https://doi.org/10.13182/FST05-A832

Seto, N., Yuki, K., Hashizume, H., & Sagara, A. (2008). Heat transfer enhancement in sphere-packed pipes under high Reynolds number conditions. *Fusion Engineering and Design*, *83*(7–9), 1102–1107. https://doi.org/10.1016/J.FUSENGDES.2008.07.044

Szanyi, M. L., Hemmingsen, C. S., Yan, W., Walther, J. H., & Glimberg, S. L. (2018). Near-wellbore modeling of a horizontal well with Computational Fluid Dynamics. *Journal of Petroleum Science and Engineering*, *160*, 119–128. https://doi.org/10.1016/j.petrol.2017.10.011

Williamson, A. S., & Chappelear, J. E. (1981). Representing Wells in Numerical Reservoir Simulation: Part 1 - Theory. *Society of Petroleum Engineers Journal*, *21*(03), 323–338. https://doi.org/10.2118/7697-PA

APPENDIX 1 – Additional Figures

Figure A1-1 Flow diagram for the IMPES solution for PDE’s, using Newton-Raphson Technique.

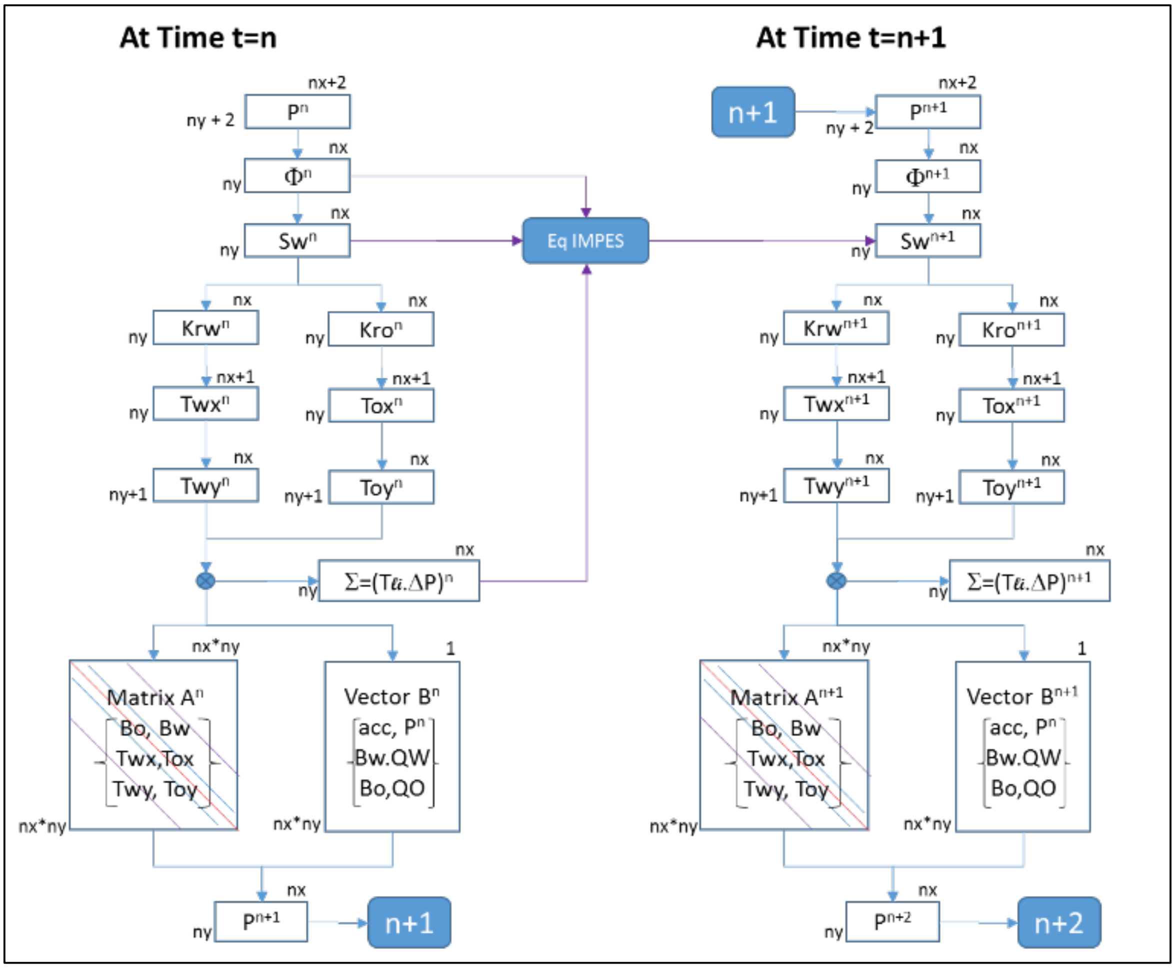

Figure A1-2. Pressure distribution occurring during constant injection rate.

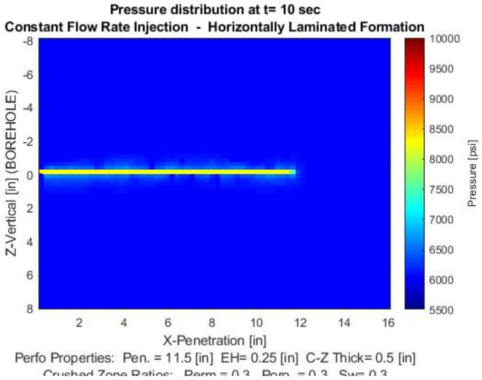

Fig A1-2a. Elapsed time = 10 sec. The simulated fluid injection at the entrance of the perforation tunnel begins to act along the walls of the tunnel. There is small pressure disturbance on the grid cells at the crushed zone level. The rest of the grid block remains at reservoir pressure of 6000 psi

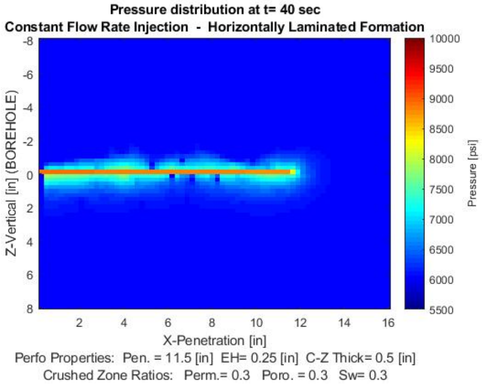

Fig A1-2b. Elapsed time = 40 sec. The pressure inside the tunnel builds up to 8000 psi. The effect of grid cells with low permeability around the tunnel is noticeable; the mass balance performed in those spots have low transmissibility, indicating that the fluid is not transmitted at the same rate as the surrounding cells with better flow transfer properties.

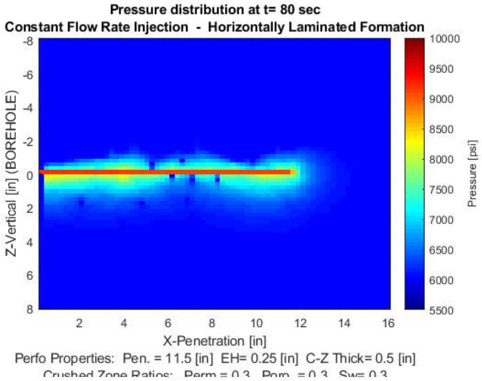

Fig A1-2c. Elapsed time = 80 sec. The pressure on the tunnel build up to 9000 psi, but is restrained by the low permeability and low porosity conditions of the crushed zone. The fluid transmission follows the areas of least resistance, indicated by higher pressure than the reservoir.

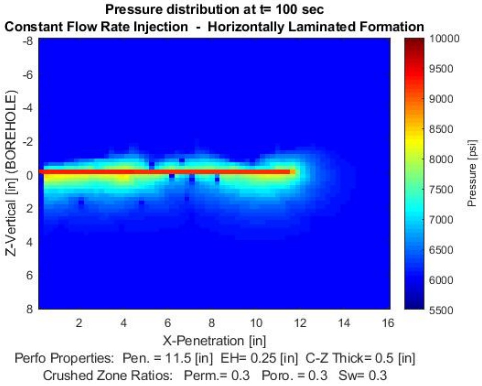

Fig A1-2d. Elapsed time = 100 sec. The effect of the fluid injected at the entrance hole is propagated into the formation. The perforation tunnel reaches a maximum pressure, that decreases towards the formation. The effect of the simulated rock grain is visible, as the assigned petrophysical properties vary the transmissibility.

Figure A1-3. Pressure distribution during constant injection rate for Horizontal Lamination formation and conductive fractures, from t=0 to t = 100 sec.

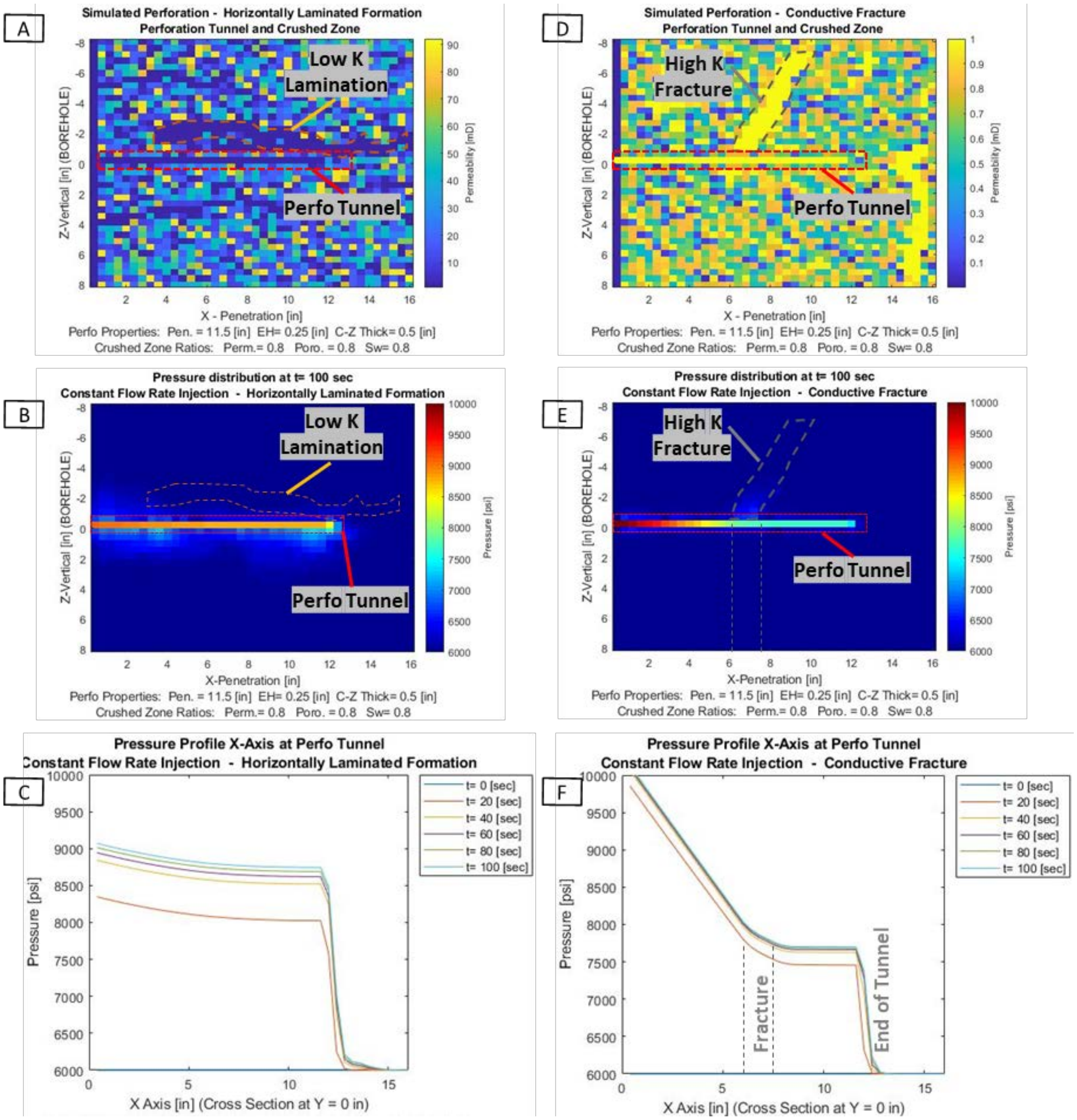

The figures on the left side correspond to a simulation of a laminated formation. **Fig A** is the distribution of the permeabilities in the grid block, designed to feature a low permeability lamination immediately above the perforation tunnel. **Fig B** is the pressure distribution after 100 s, where is observed that the pressure is only transmitted to the bottom side of the grid cell. **Fig C** is the pressure vs penetration profile in the tunnel. The pressure is evenly distributed along the tunnel. The RHS is a simulation of a conductive fracture. **Fig D** is the representation of the permeabilities. A high permeability fracture is simulated with a diagonal band intersecting with the perforation tunnel. **Fig E** shows the pressure distribution in the tunnel, but also a pressure ‘intrusion’ into the fracture. The pressure profile in **Fig F** shows a distinctive pattern where the pressure is highest at the entrance of the tunnel, and decays linearly until the point of the intersection with the fracture. After that point of the intersection, the pressure profile in the tunnel remains constant, as an indication of the injected fluid is split.

Figure A1-4. Time development for Pressure distribution, 2D mapping and surface velocity field for Dynamic Underbalance Perforation at different timing from t=0 s to t=1.0 s

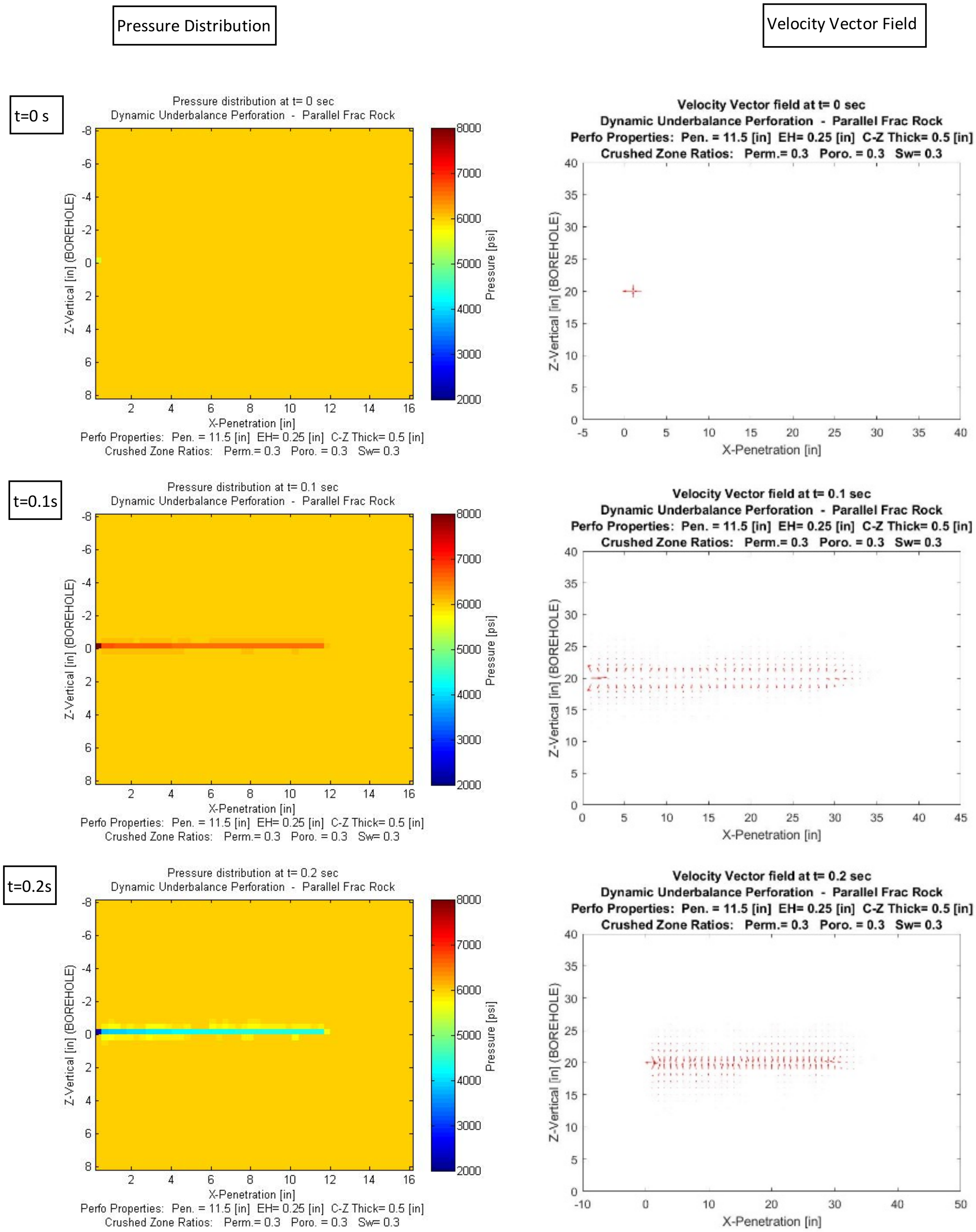

t=0.8s

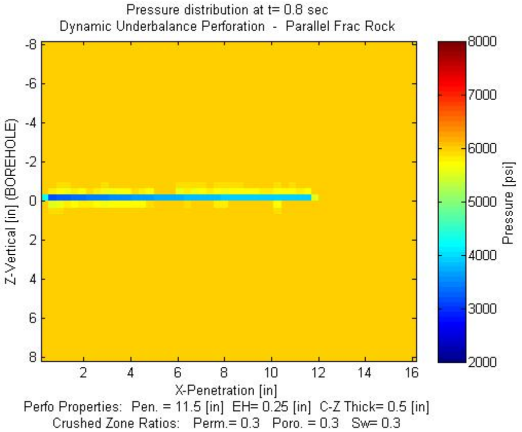
Pressure distribution at t= 0.8 sec
Dynamic Underbalance Perforation - Parallel Frac Rock
Z-Vertical [in] (BOREHOLE)
-8
-6
-4
-2
0
2
4
6
8
2
4
6
8
10
12
14
16
X-Penetration [in]
8000
7000
6000
5000
4000
3000
2000
Pressure [psi]
Perfo Properties: Pen. = 11.5 [in] EH= 0.25 [in] C-Z Thick= 0.5 [in]
Crushed Zone Ratios: Perm.= 0.3 Poro. = 0.3 Sw= 0.3

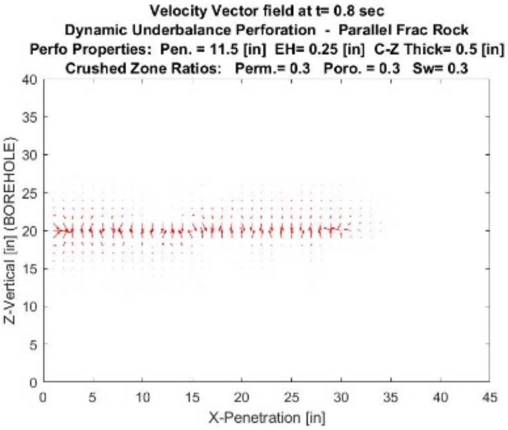
Velocity Vector field at t= 0.8 sec
Dynamic Underbalance Perforation - Parallel Frac Rock
Perfo Properties: Pen. = 11.5 [in] EH= 0.25 [in] C-Z Thick= 0.5 [in]
Crushed Zone Ratios: Perm.= 0.3 Poro. = 0.3 Sw= 0.3
Z-Vertical [in] (BOREHOLE)
40
35
30
25
20
15
10
5
0
0
5
10
15
20
25
30
35
40
45
X-Penetration [in]

t=1.0s

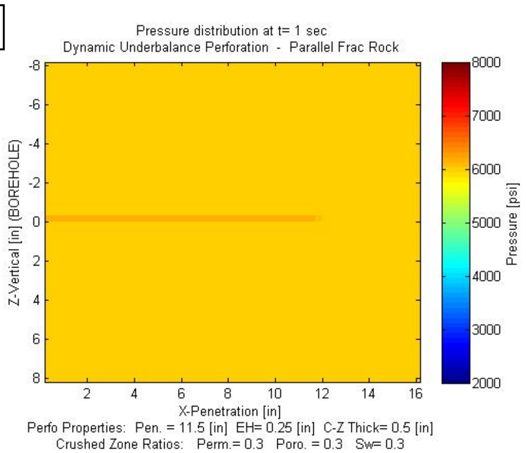
Pressure distribution at t= 1 sec
Dynamic Underbalance Perforation - Parallel Frac Rock
Z-Vertical [in] (BOREHOLE)
-8
-6
-4
-2
0
2
4
6
8
2
4
6
8
10
12
14
16
X-Penetration [in]
8000
7000
6000
5000
4000
3000
2000
Pressure [psi]
Perfo Properties: Pen. = 11.5 [in] EH= 0.25 [in] C-Z Thick= 0.5 [in]
Crushed Zone Ratios: Perm.= 0.3 Poro. = 0.3 Sw= 0.3

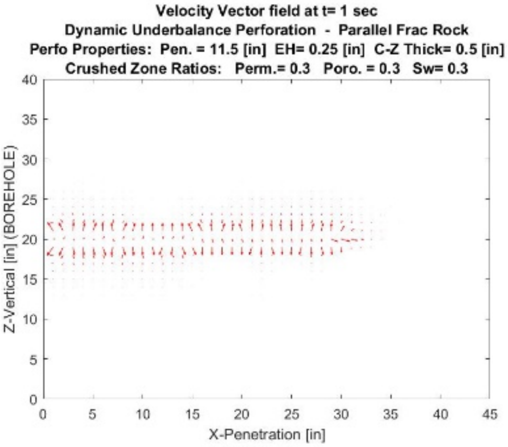
Velocity Vector field at t= 1 sec
Dynamic Underbalance Perforation - Parallel Frac Rock
Perfo Properties: Pen. = 11.5 [in] EH= 0.25 [in] C-Z Thick= 0.5 [in]
Crushed Zone Ratios: Perm.= 0.3 Poro. = 0.3 Sw= 0.3
Z-Vertical [in] (BOREHOLE)
40
35
30
25
20
15
10
5
0
0
5
10
15
20
25
30
35
40
45
X-Penetration [in]

APPENDIX 2 – Mathematical derivation of the simulator

A2.1 Material Balance Equations

The mass balance equation is written in terms of flow rate, by defining the mass flow rate *m [kg/s]* as the product of flow rate *[m^3/s]* and density *[kg/m^3]*. The mass balance equation in two dimensions over a definite interval *Δt*, can be expressed as **Eq A2-1**.

$$\left[(m)_{x-\frac{\Delta x}{2}}\Delta t + (m)_{y-\frac{\Delta y}{2}}\Delta t\Delta t\right] - \left[(m)_{x+\frac{\Delta x}{2}}\Delta t + (m)_{y+\frac{\Delta y}{2}}\Delta t\Delta t\right] + m_s\Delta t = (\phi\rho\Delta x\Delta y)_{t+\Delta t} - (\phi\rho\Delta x\Delta y)_t \text{ ,..(A2-1)}$$

Referring to **Fig 3-B**, the first two terms in **Eq. A2-1** represents the amount of mass that flows into -m_{in}- and out -m_{out}- of the control volume. For x-axis, such in and out flow occur at walls located at *x-Δx/2* and *x+Δx/2* respectively. Similar analysis can be done for *y* and *z* axis. The term $q_m\Delta t$ refers to the volume that is extracted from –'sink'- or added to –'source'- the system, and the terms on the right-hand side are the accumulated mass – 'm_a'- within the control volume, calculated as the fraction occupied by the fluid in the rock volume over the period *Δt*.

The mass flux *[kg/(s.m^2)]* is defined as mass per unit time per unit area, and can be written in terms of density *ρ* and volumetric velocity *u* as

$$\dot{m}_i = \alpha_c\rho u_i \text{ , …….(A2-2)}$$

The Mass flow rate *m* can also be expressed as the $_{\text{mass}}$ flux over the area on the control volume wall A_x=$\Delta_y\Delta_z$

$$m = \dot{m}_i A_x \text{ , ………………………………………………………..(A2-2)}$$

Applying the concept of differentiation when the control volume dimension and time increment are taken to limit approaching zero, the equation results in

$$-\frac{\partial}{\partial x}(\rho u_x A_x)\Delta_x - \frac{\partial}{\partial y}(\rho u_y A_y)\Delta_y + \frac{q_m}{\alpha_c} = \frac{V_b}{\alpha_c}\frac{\partial}{\partial x}(\phi\rho) \text{ , ……...(A2-3)}$$

By taking definitions of Darcy law for flow through porous media, the superficial velocity can be expressed as

$$u_x = -\beta_c\frac{k_x}{\mu}\frac{\partial\varphi}{\partial x} \text{ ………….(A2-4)}$$

Also, the mass rate is expressed as flow rate

$$q_m = a_c q_{sc}\rho_{sc} \text{ …..(A2-5)}$$

Combining **Eq A2-3 and A2-4**, it is obtained the governing equation for reservoir engineering applications:

$$\frac{\partial}{\partial x}\left[\beta_c K_x A_x\frac{K_{ro}}{\mu_o B_o}\left(\frac{\partial P_o}{\partial x}\right)\right]\Delta_x + \frac{\partial}{\partial y}\left[\beta_c K_y A_y\frac{K_{ro}}{\mu_o B_o}\left(\frac{\partial P_o}{\partial y}\right)\right]\Delta_y = \frac{V_b}{a_c}\frac{\partial}{\partial t}\left(\frac{\phi\, S_o}{B_o}\right) - q_{osc}, \text{ …..(A2-6)}$$

The flowing conditions within the rock are determined by the Transmissibility term, which considers the petrophysical and fluid mechanical properties of the rock. The transmissibility must be written for each phase (oil and water) and direction (vertical and horizontal) by using the equation.

$$T_{lx} = \beta_c K_x A_x\frac{K_{rl}}{\mu_l B_l} \text{ , ………………………………..(A2-7)}$$

Where *l* indicates the phase (oil or gas) and *x* indicates the orientation (vertical or horizontal) K_x is the arithmetic average of permeability between adjacent grid cells, A_x is the area of flux, Kr_l is the relative permeability, μ_l is the fluid viscosity and B_i is the formation factor (since all calculations occur downhole, formation factor can be considered as B=1). In other words, four different values for transmissibility will be calculated: *Twx, Tox, Twy* and *Toy*.

The right hand side of Eq A2-6 can be expressed in terms of increase of Porosity and Saturation at each time step Δt

$$\frac{\partial}{\partial t}\left(\frac{\phi\, S_o}{B_o}\right) \approx \frac{1}{\Delta t}\Delta t\left(\frac{\phi\, S_o}{B_o}\right), \ldots\ldots\ldots\ldots\ldots\ldots\ldots\ldots\ldots\ldots\ldots\ldots\ldots\ldots (\,A2\text{-}8\,)$$

By considering definitions for porosity and water saturations, an equation to calculate water saturation at the NEXT TIME STEP $S_w^{\,n+1}$ explicitly is obtained in **Eq A2-9**:

$$\phi^{n+1} S_w^{n+1} = \left\{\phi^{n+1} - \phi^{n}(1 - S_w)^{n} - [\Sigma(T_o \Delta P_o + q_o)]\left[\frac{1}{\frac{V_b}{a_c \Delta t B_o}}\right]\right\}, \ldots\ldots\ldots\ldots (\,A2\text{-}9\,)$$

Rearranging **Eq A2-8 and A2-9** by grouping the next step pressures components P^{n+1} in the left-hand side of the equation, it is obtained a final equation for the 2D model is of the form

$$(\boldsymbol{S}_{i,j})(P_{i,j-1}^{n+1}) + (\boldsymbol{W}_{\boldsymbol{i,j}})(P_{i-1,j}^{n+1}) + (\boldsymbol{C}_{\boldsymbol{i,j}})(P_{i,j}^{n+1}) + (\boldsymbol{E}_{\boldsymbol{i,j}})(P_{i+1,j}^{n+1}) + (\boldsymbol{N}_{\boldsymbol{i,j}})(P_{i,j+1}^{n+1}) = -(\boldsymbol{D}(P_i^{n}) + B_w q_{w,i} + B_o q_{o,i}\,), \ldots\ldots\ldots\ldots\ldots\ldots\ldots\ldots\ldots\ldots\ldots\ldots (\,A2\text{-}10\,)$$

Where:

$$\boldsymbol{S_i} = B_w T_{w,j-} + B_o T_{o,j-}$$

$$\boldsymbol{W_i} = B_w T_{w,i-} + B_o T_{o,i-}$$

$$\boldsymbol{C_i} = B_w T_{w,i+} + B_w T_{w,i-} + B_o T_{o,i+} + B_o T_{o,i-} + \frac{V_b \phi_o C_f}{a_c \Delta t}$$

$$\boldsymbol{E_i} = B_w T_{w,i+} + B_o T_{o,i+}$$

$$\boldsymbol{N_i} = B_w T_{w,j+} + B_o T_{o,j+}$$

$$\boldsymbol{D} = \frac{V_b \phi_o C_f}{a_c \Delta t} \quad ..\ Constant$$

The terms *Si, Wi, Ei* and *Ni* are the transmissibility terms for the adjacent cells, with respect to ‘current’ grid cell *Ci*, as illustrated in **fig A2-1.**

	N_1			
W_1	C_1	E_1		
	S_1			

Figure A2-1 Nomenclature of the current cell and neighboring cells for mass balance equation for each grid cell

Each grid cell will produce a linear equation of the form as eq A2-10. Therefore a grid represented in a matrix of n_x x n_y dimension, will have $n_x . n_y$ equations and same number of unknowns ($P_{i,j}^{n+1}$).

Arranging the set of equations in matrix form, will take the form *Ax=b*, as in ***fig A2-2.***

$$\begin{bmatrix} C_1 & E_1 & 0 & 0 & N_1 & 0 \\ W_2 & C_2 & E_2 & 0 & 0 & N_2 \\ 0 & W_3 & C_3 & E_3 & 0 & 0 \\ 0 & 0 & W_4 & C_4 & E_4 & 0 \\ S_5 & 0 & 0 & W_5 & C_5 & E_5 \\ 0 & S_6 & 0 & 0 & W_6 & C_6 \end{bmatrix} \mathrm{x} \begin{bmatrix} P_1^{n+1} \\ P_2^{n+1} \\ P_3^{n+1} \\ P_4^{n+1} \\ P_5^{n+1} \\ P_6^{n+1} \end{bmatrix} = \begin{bmatrix} -D.P_1^{n} - q_1 \\ -D.P_2^{n} - q_2 \\ -D.P_3^{n} - q_3 \\ -D.P_4^{n} - q_4 \\ -D.P_5^{n} - q_5 \\ -D.P_6^{n} - q_6 \end{bmatrix}$$

Figure A2-2. Known flow rate Q – Calculate for next step P_6^{n+1}: Arrangement for Matrix coefficient A, unknowns vector X and knowns vector b.

The implicit solution of the equation *Ax=b* will produce a vector *x*, that will contain the NEXT STEP PRESSURES $P_{i,j}^{n+1}$ for each grid cell within the matrix.

A2.2 Numerical method description

The approach is for the simulator to solve the partial differential equations for mass balance by using Newton Raphson linearization, and implicit explicit (IMPES) method to solve for the NEXT STEP PRESSURE for each grid block. Initial conditions are set for boundary and system conditions, the initial pressure on each cell of the grid P_i^n, and a driving force (flowrate Q at sink/source point) *AT CURRENT TIME [n]*, to iterate on the mass balance equations to find the *new* set of pressure values P_i^{n+1} for the system *AT NEXT TIME STEP [n+1] as represented in the schematics of **fig A2-3***.The iteration is repeated to a number of acceptable time steps, depending on the nature of the work to be simulated. For the case of perforations, the fluid dynamics occur within few seconds after perforation guns are detonated, therefore the time steps are in the order of seconds, whereas production or stimulation jobs can take minutes or hours.

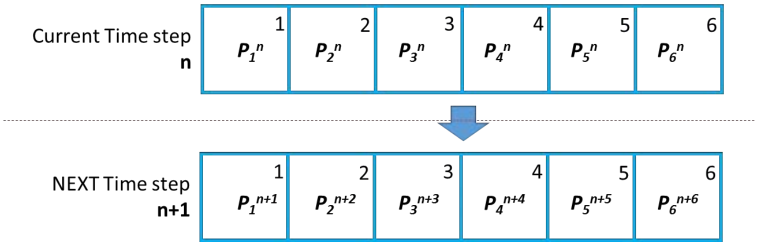

Figure A2-3 - A row of grid cells (1-Dimension Gridblock) at the current time step P_i^n and the calculated next step pressures P_i^{n+1}.

A2.3 Boundary conditions

The external border of the grid must be considered as open flow or Constant-Pressure boundary. To model that boundary condition, the original grid size *(Nx,Ny)* is imposed over a 'ghost' or 'fictitious' matrix of size *(Nx+1,Ny+1)* as described in (Ertekin, Abou-Kassem and King 2001) . The fictitious matrix is a set of external sink/source gridlocks at constant formation pressure that compensates for fluid transfer within the grid. In other words, it doesn't restrict the flow transfer as opposed to No-Flow boundaries. The fictitious matrix is the numerical representation of an infinite reservoir at a given formation pressure. The x=0 line corresponding to well completion (cemented casing) the permeability is set to (near) 0 mD.

A2.4 The Algorithm

The objective of the algorithm is to find implicitly the pressure values in each grid cell at the next time step *N+1*. In order to reach that goal, a matrix *A* is formed as described previously. Once the next step pressures P_i^{n+1} have been calculated, the Next step water saturation Sw_i^{n+1} is calculated explicitly by using equation 13. The combination of *implicit* on Saturation and *explicit* on Pressure is called IMPES method.

The algorithm starts by assuming that all the grid blocks are at constant pressure at current time step N. Initial pressure *P*, Water Saturation *Sw*, Grid Permeabilites *K* and Relative Permeability *Krx* relations are defined by the user. Based on the initial grid properties, the transmissibility term includes the petrophysical properties that regulate how easy or difficult is to transfer fluid between adjacent cells. Transmissibility is calculated by using **eq A2-7**.

A2.5 Alternative Solution: Provided pressure – Solving for Flow Rate

A common approach in petroleum engineering is to use a sink/source driving force with a defined pressure-time, instead of defined flow rate Q. Since the analysis of this paper is to evaluate the response of the fluid at the crushed zone to a pressure pulse, it is therefore necessary to perform the flow calculations based on the magnitude of the pressure pulse.

Within the reservoir modelling framework, a common approach is to use Darcy reservoir equations (Williamson and Chappelear 1981) that calculate the flow rate based on the differential pressure between reservoir pressure and flowing pressure, applied on a scenario where the effective reservoir radius (boundary of the grid cell) is considerably larger than the well radius ($r_e >> r_w$). The area of flow for Darcy equation equals the cylindrical surface area of radius r_w (wellbore) and height *h* (pay zone). By using this approach on a small scale grid size would be incorrect, given that the flow area is of the same size of the grid cell ($r_w = r_e$),.

In order to overcome the conflict of the conventional concept, a different approach is needed. Based on the developed mass balance equation (**Eq A2-10**), the pressure term corresponding to the sink/source point (perforation tunnel entrance hole) will be known at every time step ($P_{i,j}^N$).

The alternative proposed method in this paper for calculating the flow rate Q from a given Pressure response, at sink/source point consist of taking advantage that the entire pressure transient in the borehole are known at every time step.

This pressure transient will be applied only at the sink/source grid cell, corresponding to the cell where the entrance hole of the perforation is located.

For simplicity a 1-D linear grid is described, assuming that the SINK/SOURCE point is at cell i=3. The mass balance equation in terms of pressure is:

$$(\boldsymbol{W})(P_2^{n+1}) + (\boldsymbol{C})(P_3^{n+1}) + (\boldsymbol{E})(P_4^{n+1}) = -\boldsymbol{D}(P_3^n) - Bi\ Q_3\ , \dots\dots\dots\dots\dots\dots\dots\dots\dots\dots\dots \textit{(A2-11)}$$

In this case, the Pressure at grid block i=3, for current time step $P^n{}_3$ and next step $P^{n+1}{}_3$ is already known. The unknowns are the next step pressure for neighboring cells $P^{n+1}{}_2$ and $P^{n+1}{}_4$, and the flow rate q_3. Eq A2-11 can be rearranged as:

$$(\boldsymbol{W})(P_2^{n+1}) + Bi\ Q_3 + (\boldsymbol{E})(P_4^{n+1}) = \quad -\boldsymbol{D}(P_3^n) - (\boldsymbol{C})(P_3^{n+1})\ , \dots\dots\dots\dots\dots\dots\dots \textit{(A2-12)}$$

Following the same procedure for each cell, the matrix can be built, where the total sink/source flow rate at current step Q^n becomes part of the unknowns, and solved as part of the set of equations $Ax=b$. In the context of finding solution to the set of equations $Ax=b$ as expressed in **fig A2-4**, the pressures at current and next time step ($P_{i,j}^n$ and $P_{i,j}^{n+1}$) *of the sink/source point* will become part of the known variables *b vector*, and the flow rate at the sink/source point will be included within the unknowns *x vector.*

The resulting matrix can be expressed in the form as **fig A2-4**

$$\begin{bmatrix} C_1 & E_1 & 0 & 0 & N_1 & 0 \\ W_2 & C_2 & \mathbf{0} & 0 & 0 & N_2 \\ 0 & W_3 & \mathbf{Bi} & E_3 & 0 & 0 \\ 0 & 0 & \mathbf{0} & C_4 & E_4 & 0 \\ S_5 & 0 & 0 & W_5 & C_5 & E_5 \\ 0 & S_6 & 0 & 0 & W_6 & C_6 \end{bmatrix} \mathrm{X} \begin{bmatrix} P_1^{n+1} \\ P_2^{n+1} \\ Q_3^{n} \\ P_4^{n+1} \\ P_5^{n+1} \\ P_6^{n+1} \end{bmatrix} = \begin{bmatrix} -D.P_1^{n} \\ -D.P_2^{n} - E_2.P3^{n+1} \\ -D.P_3^{n} - C_3.P3^{n+1} \\ -D.P_4^{n} - W_4.P3^{n+1} \\ -D.P_5^{n} \\ -D.P_6^{n} \end{bmatrix}$$

Figure A2-4 Arrangement for Matrix coefficients when Pressure P is known and Calculate for Flow Rate Q: Matrix, unknowns vector P^{n+1} *and knowns vector* P^{n}.

The term *Bi* is the formation volume factor coefficient inherent to flow rate *Q*. Since all calculations are downhole, this *Bi* factor equals 1.

By using the mathematical approach to derive the current step Flow Rate Q_i^n, it is provided an alternative technique to calculate directly from the mass balance equation. The only setback of this method is that a TOTAL FLOW RATE *Q* is calculated. (i.e., it cannot be segregated into each phase contribution by oil or water). A similar approach is discussed in textbooks (Ertekin, Abou-Kassem and King 2001) but it does not provide the mathematical solution.

A2.6 Nomenclature in Appendix 2

The following variables are introduced in appendix 2. (Additional to the terms described in the main script nomenclature)

$T_{l,d}$	Transmissibility l = fluid (o: oil, w: water), d = direction of fluid transfer (x, y coordinates)

Equation index for grid cells, according to relative location within the network:

S	South
W	West
C	Center
N	North
E	East
D	Solution vector coefficient

APPENDIX 3 – Analysis of Grid Block Size and Time Step

For the purposes of this discussion, the concept of stability in a numerical solution refers to the comparison of the calculated value at a specific point, obtained with grid cells of different size and number of time steps for each iteration, while keeping other parameters constant. The system used for this work is Intel Xeon CPU E5 2680 v3 @ 2.65 GHz.

Grid Block Size Analysis

The objective of the analysis is to determine whether the solution of the system is consistent for the different grid cell sizes; but it is also important to know the computing resources needed to find an efficient solution, before the grid size becomes prohibitively costly in terms of computing power.

The selected point for the analysis is the tip of the perforation tunnel simulated on a homogenous formation, for N = 35, 40, 50, 60 and 70 cells. (The grid block size is N^2)

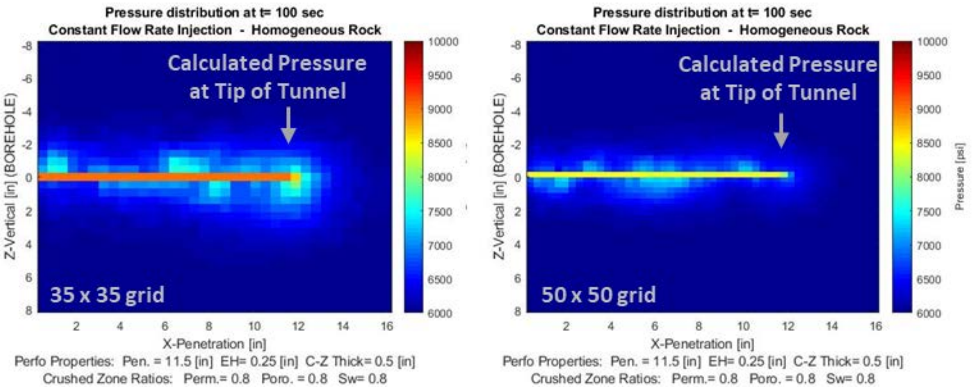

Fig A3-1 Simulated grid sizes of 35x35 and 50x50, used in the Grid Block Size Analysis. The computed pressure at the tip of the tunnel is used as reference to evaluate the consistency of the results.

The results are plotted in **Fig A3-2** below. The pressure at the end of the tunnel is measured at 9006 psi for a 35 x 35 grid block, taking 30.8 sec computing power. For the case of a grid block of 60x60 and 70x70, the calculated pressures are 7680 and 7254 psi, respectively, with computing time of 267 and 569 seconds. As observed from the plot, increasing the grid size reduces the variation in the pressure calculation, but the computing time increases exponentially.

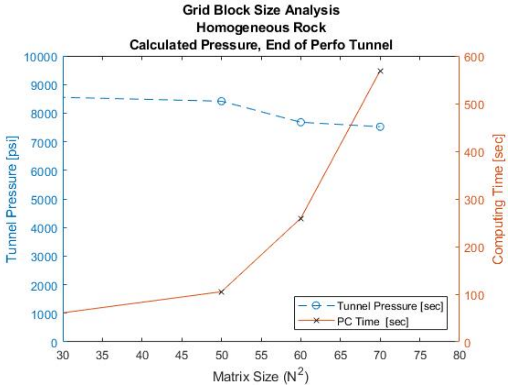

Fig A3-2. Comparison of the calculated pressure by using different grid block sizes. The pressure tends to stabilize to a constant value as the grid size increases. On the other hand, the computing time increases exponentially, resulting in computing-costly iterations.

Time Step Stability Analysis

The number of time steps (NTS) used in the calculations in this paper was defined based on the time step stability. The stability analysis was done based on the pressure calculated in a specific spot – selected at the tip of the tunnel – with the number of time steps as the dependent variable. The concept of stability in this analysis refers to the evaluation of the consistency and repeatability of the solutions of the numerical simulation.

Each iteration is run for a total event duration T [sec], based on the time frame that is expected for the simulated operation. For instance, considering a dynamic underbalance scenario, the duration of the event lasts only few seconds, whereas injection or production operations may last minutes or hours. The time step DT, -or time increment used in each iteration of the newton Raphson model method- is calculated DT=T/NTS [sec].

Increasing the number of time steps NTS produces a shorter time increment DT, which is therefore is expected to produce a more accurate solution. On the other hand, a reduced NTS is desired since it will maintain a low computational overhead; but this shouldn't compromise the stability of the numerical simulation.

The different iterations over a range of NTS is plotted in **Fig A3-3**. The horizontal axis is the NTS, increasing from 10 to 100. The primary vertical axis is the pressure calculated at the tip of the tunnel. The secondary vertical axis is the computational time required to complete the iteration. Additionally, calculations for total iteration time T of 20, 50 and 100 sec are shown to observe the variation for different time durations.

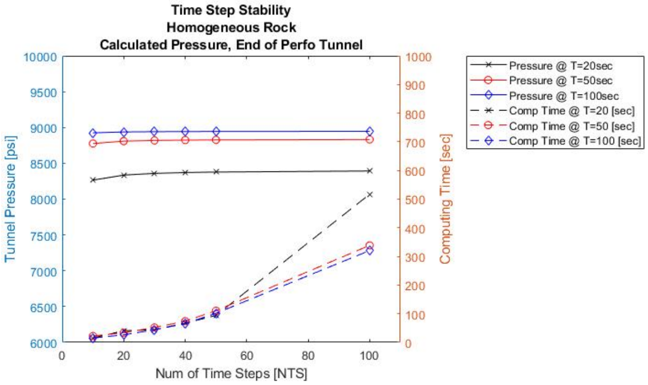

Fig A3-3. Analysis of the stability of increasing the number of time steps (NTS). NTS defines the size of the time increment ΔT used in the numerical solution. For small NTS (large ΔT), the calculated pressure is not consistent, seen as increase in the curve, therefore the system is assumed to be unstable. After NTS=40, the computed pressure is maintained within <2% of the total reading, and at a reasonable low computing time.

For the total event Time of T=20s (black solid line with cross markers), the pressure calculated with NTS=10 is 8265 psi. Increasing NTS to 20, the calculated pressure is 8335 psi. This increment in pressure is considerable, then is may be considered that the time step is not stable. Repeating the iteration with NTS values of 40, 50 and 100, the resulting calculated pressure at same spot at the tip of the tunnel is 8371, 8378, and 8383 psi, respectively. The Pressure increments from 8371 to 8383 psi is 12 psi, which is 0.14% of the total reading. Analyzing the Computing time (black dashed line with cross markers), the iteration NTS=40 takes 67 s, (with the afore mentioned computing power), whereas the NTS=100 requires computation time of 517 sec. The considerably higher computing time does not represent a substantial improvement in the final pressure result; therefore, it can be assumed NTS=40 as stable and efficient time step.

Similar analysis done for different duration events T = 50 and 100 s shows that after the NTS = 40 the calculated pressure stabilizes to a constant pressure for the three different simulated event duration.

Engineering practices will be required to assess the margin of error in the solution, by keeping reasonable computing processing time considering available resources. The implications of the restrictions of the grid cell and number of time steps in the resolution relate to the rock grain size and its petrophysical properties that are modeled by the proposed fluid mechanics near borehole simulator.

ARTICLE 2.

ANALYSIS OF NEW RP 67 RECOMMENDED SAFETY DISTANCES FOR 50-OHM RESISTORIZED AND RF-SAFE DETONATORS

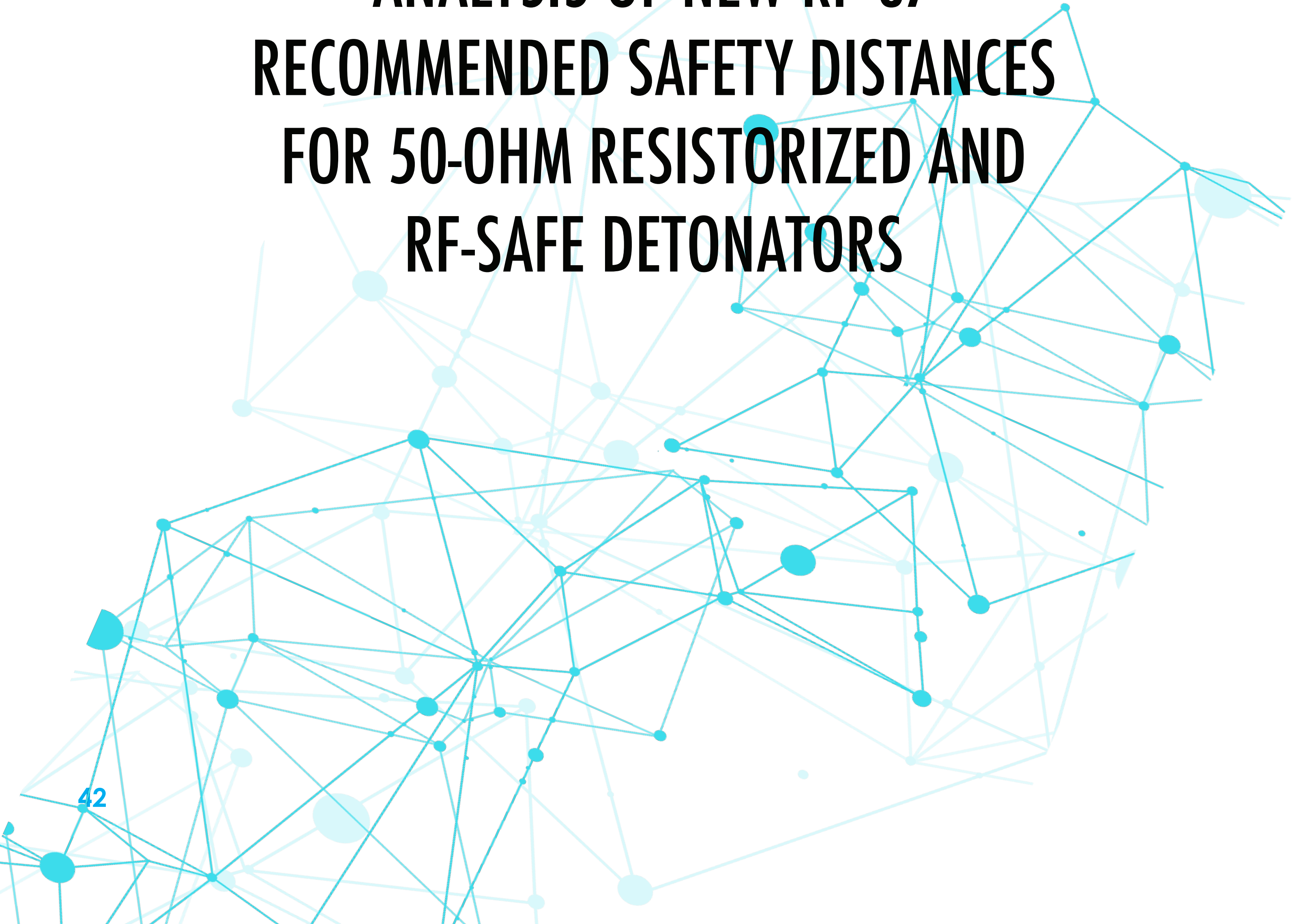

COVER SHEET

Analysis of New RP 67 Recommended Safety Distances for 50-Ohm Resistorized and RF-Safe Detonators

Authors:
Ryan Brady, DynaEnergetics
Andreas Zemla, DynaEnergetics
Liam McNelis, DynaEnergetics

Ryan Brady, Product Line Manager TCP/Hardware/Initiation Systems
Joined DynaEnergetics in 2018 as PLM for TCP and Hardware systems. Prior to DynaEnergertics I joined Halliburton in 2007. Throughout my career at Halliburton I worked multiple positions including Business Development and Global TCP Product Champion. Most previous position was Sr Technical Advisor TCP for Halliburton Energy Services located on the North Slope Ak.Co-Authored SPE SPE-166238-MS "Frac-Perforating Charge Maintains Treating Pressure while Increasing Pumping Rate: A Case Study in South Texas" and presented at SPE ATCE October 2013.

Andreas Zemla, Manager New Product Development and Electronic Systems
Education to telecommunication electronic technician at the German Telekom Study at the German Telekom University for applied science for electronic and telecommunication in Dieburg. R&D Engineer for Hard and Software design at Dynamit Nobel Explosivstoff und Systemtechnik GmbH for 6 years R&D Engineer and Product Manager for electronic initiation systems for military and defense at DynITEC GmbH for 13 years. Since 2015 Manager New Product Development and Electronic Systems at DynaEnergetics GmbH

Liam McNelis, Vice President of Research & Development. Liam McNelis joined DynaEnergetics in 2003 as an R&D Engineer. In 2009, he assumed the role of R&D manager at DynaEnergetics and was promoted to R&D Director in 2018. He is currently responsible for the global R&D activities within the company. In 2004, he obtained a German explosives license, is a member of SPE and is an inventor on several oilfield patents. Previous to joining DynaEnergetics, Liam worked for Aixtron AG, as a process engineer for CVD equipment for the semiconductor industry. He holds an engineering degree from the University of Dublin, Trinity College.

JIPF, Vol. 3 Issue 1, FEBRUARY 2020

Analysis of New RP 67 Recommended Safety Distances for 50-Ohm Resistorized and RF-Safe Detonators

Ryan Brady, DynaEnergetics; Andreas Zemla, DynaEnergetics; Liam McNelis, DynaEnergetics

Executive Summary

Multistage plug-and-perf operations can present many hazards, specifically as it pertains to electrical and electronic detonators. There are often multiple sources of radio frequency (RF) transmissions present during various aspects of the operation, particularly with the increase in zipper fracturing jobs, where wireline often works in sequence with pumping processes. To successfully complete these projects, constant communication between the pumping operators and the tech command center (TCC) is required.

Communicating with RF transmitters, among other electromagnetic sources, can potentially increase the risk of detonators firing prematurely. Traditionally, perforating guns were armed with resistorized detonators with mechanical or addressable safety switches. Although safer than non-resistorized detonators, these guns can still be susceptible to inadvertent detonation from induced stray current. Due to this risk, jobsites have required radio silence, resulting in a significant amount of lost time.

In this article, we will describe how the various sources of electromagnetic radiation can affect Group 1 resistorized detonators and Group 2 RF-safe detonators. The safe distances between the detonator and the transmitter will also be described, detailing what is quantifiable when a detonator leaves the safe-state.

1. Background and Introduction

Regulations and safety procedures for perforating guns are governed by the American Petroleum Institute (API) and the Pipeline and Hazardous Materials Safety Administration (PHMSA). The API details safety standards through RP 67: *Recommended Practice for Oilfield Explosives*[1], while PHMSA regulates the transportation and storage of "jet perforating guns (JPG)" to wellsites through Hazard Materials Regulations (HMR), 49 CFR[2]. Both sets of guidelines have been updated multiple times, affecting operators and service companies, with regards to safely providing perforating products and services.

Initially published in 1994, API RP 67 was revised in 2007, and again in 2015. A fourth edition[3], awaiting approval, will introduce strict standards for safely arming detonators away from RF signals. This edition introduces three groups of detonators. Group 1 detonators require RF-exclusion zones, while Group 3 "immune" detonators do not. However, due to their high cost and complexity, Group 3 detonators are difficult to adopt for oilfield operations and are more suitable for military applications to control the firing of missiles, torpedoes and other precision-guided ordnance.

Because of the RP 67 best practices, many service companies strive to have their detonators, or select-fire systems fit into the Group 2 "safe" category. This group requires a much smaller RF-exclusion zone and is seemingly made safe by including an electronic switch that is installed before the resistorized detonator.

Under this provision, the guns can be armed at the gun-loading facility and transported to the wellsite with approval from PMSHA. However, at the end of 2018, PMSHA published updated guidelines that restrict transporting JPGs with installed detonators. With the new update, each JPG with an installed detonator must have a safety-interrupt integral to the detonator, not just an electronic safety switch. The gun also must be verified by an independent third party, typically the wireline service provider.

In short, any company shipping JPGs with installed detonators is required to submit third-party test results to achieve compliance. PMSHA is currently allowing the service providers or wireline companies to self-govern and submit certifications in good faith.

Not only do the new RP 67 guidelines affect how loaded JPGs are shipped, they also provide an updated table for safely arming JPGs on location. According to the RP 67 fourth edition, Group 2 detonators should have a no-fire voltage of 25V AC/DC. RF-safe distances are detailed by the Institute of Makers of Explosives (IME) in *SLP 20: Safety Guide for the Prevention of Radio Frequency Radiation Hazards in the Use of Commercial Electric Detonators (Blasting Caps)*[4].

Under the new guidelines, detonator RF sensitivity for each single transmitter identified in SLP 20 must be evaluated, and its table of safe distances published. These must be supplied to all users by the manufacturer. The safety-related features and characteristics must be tested by an independent third-party organization (ITPO).

To pass, the system must demonstrate no unintended detonation with a single point of failure, as evidenced by a systematic analysis of failure mode (FMEA). With these new standards in place, manufacturers must determine how to test the components and quantify the previously mentioned safety standards.

2. **Detonator Testing**

For the purpose of these tests, an electronic detonator is defined as being an initiating device with an electronic subassembly or electronic board between the input side of the detonator and its fuse, which is in close vicinity to the primary and secondary explosive loads. The electronic subassembly functions as a protective element against extraneous power/electricity and electromagnetic–induced energy that may influence the fuse head of the detonator. The electronic subassembly/electronic board controls the fuse head of the detonator fire by communicating with the overriding device or firing panel, which sends a specific digital signal to the detonator. As part of its function as a protective element, the electronic subassembly board is intended to eliminate or reduce the coupling of electromagnetic radiation into the detonator's fuse head. Under certain extreme conditions, depending on field strength, electromagnetic radiation can permeate the detonator lead wires and the electronic subassembly, affecting the fuse head.

Under this aspect, one must consider at which level of induced energy is the detonator still safe. To determine this, the electrical characteristics of the fuse head and the no-fire current values of the fuse were considered and a safety factor of -17dB was included.

This means approximately one-eighth or 12.5% of the no-fire-current value is used as the critical value to quantify when the detonator is still safe. Using this as a benchmark, the detonator is still in a safe-state even if a current up to a level of one-eighth of the no-fire current is induced in the fuse head by electromagnetic radiation. The electromagnetic radiation, as defined by the transmission frequency, and the corresponding field strength, can have different influences on the detonator depending on which frequency the detonator is exposed to at different field strength levels. For this reason, it is essential to measure the induced current in the fuse head across all frequencies.

The worst-case scenario, or rather the most unfavorable positioning of the detonator lead wires, must be applied to the tests when exposing the detonators to the electromagnetic radiation. In this case, a lambda ¼ dipole antenna was formed by bending the lead wires of the detonators accordingly. This is shown in Fig. 1.

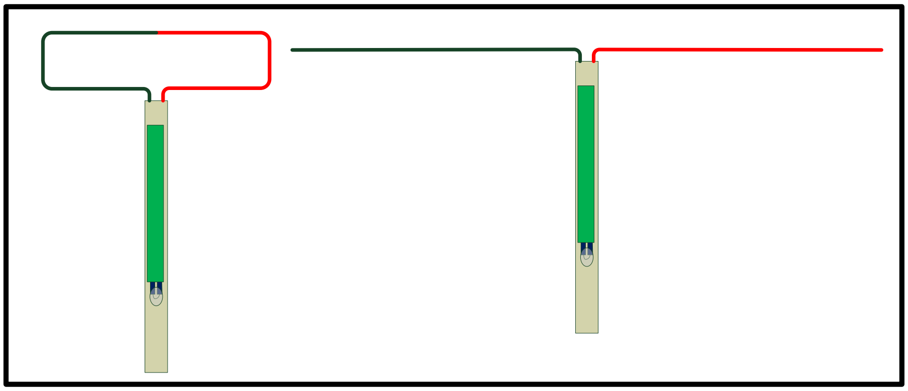

Fig.1. Lambda ¼ dipole antenna.

In the SLP 20 test procedure, radio transmitters are listed in a table with different frequencies and transmission powers. Using the data on the transmission power, it is possible to calculate a distance to the detonator that is still safe. To calculate practical safe distances, the field strengths at all frequencies where the detonator is still in a safe-state were measured; whereby, the most unfavorable dipole antenna shaped of the lead wires was formed. The current measured in the fuse head of the detonator must not exceed 12.5% of the no-fire current value during these measurements. The test set up is illustrated in Fig 2.

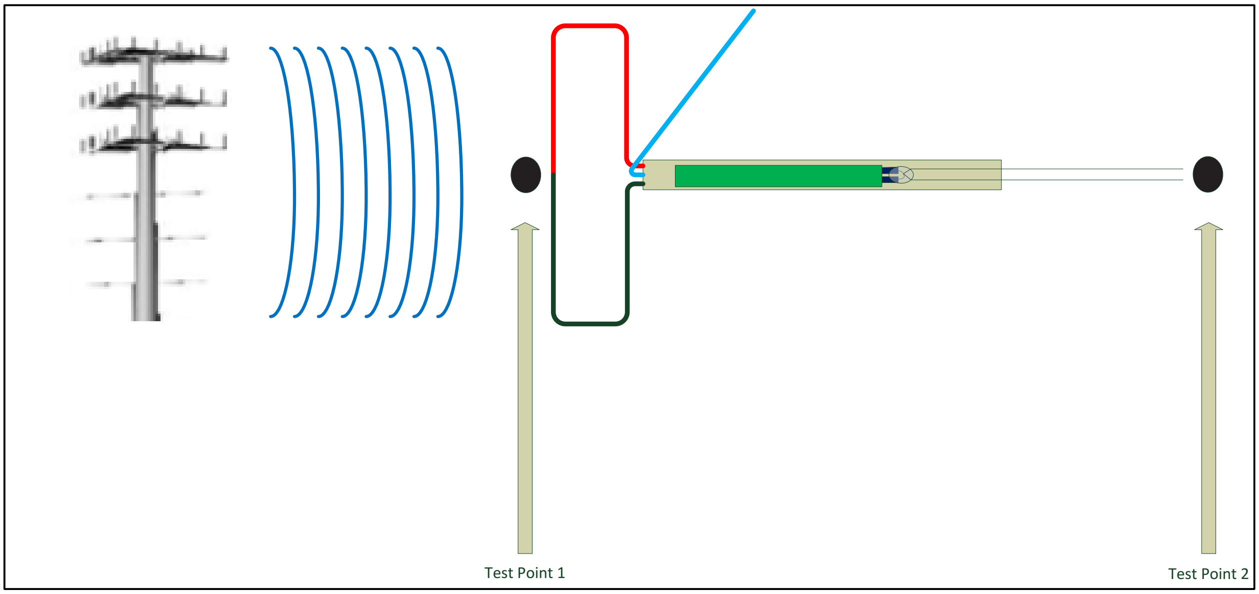

Fig. 2. SLP 20 test setup.

At the Test Point 1, in Fig. 2, the field strength was measured for each corresponding transmission frequency, while the parallel induced current in the detonator fuse head was measured at Test Point 2.

The field strength was increased until the measured current at Test Point 2 reached the critical reference point of 12.5% of the no-fire current level for the fuse head. This was carried out with the lead wires of the detonator in the worst-case position, and all measurements were conducted in all three-dimensional axis and with both polarities (horizontal and vertical).

Example. At a frequency of 10 MHz, the detonator was radiated and exposed to a field strength of 300 V/m with both polarities and was measured in a three-dimensional axis. The measured induced current at the fuse head was below 12.5% of the no-fire current value.

In the frequency range of 1 to 2 GHz, the field strength had to be reduced to 100 V/m for the induced current at the fuse head to be below 12.5% of the no-fire current value.

After completing the measurements for all frequency ranges, the following set of data was available in order to calculate the corresponding safety distances.

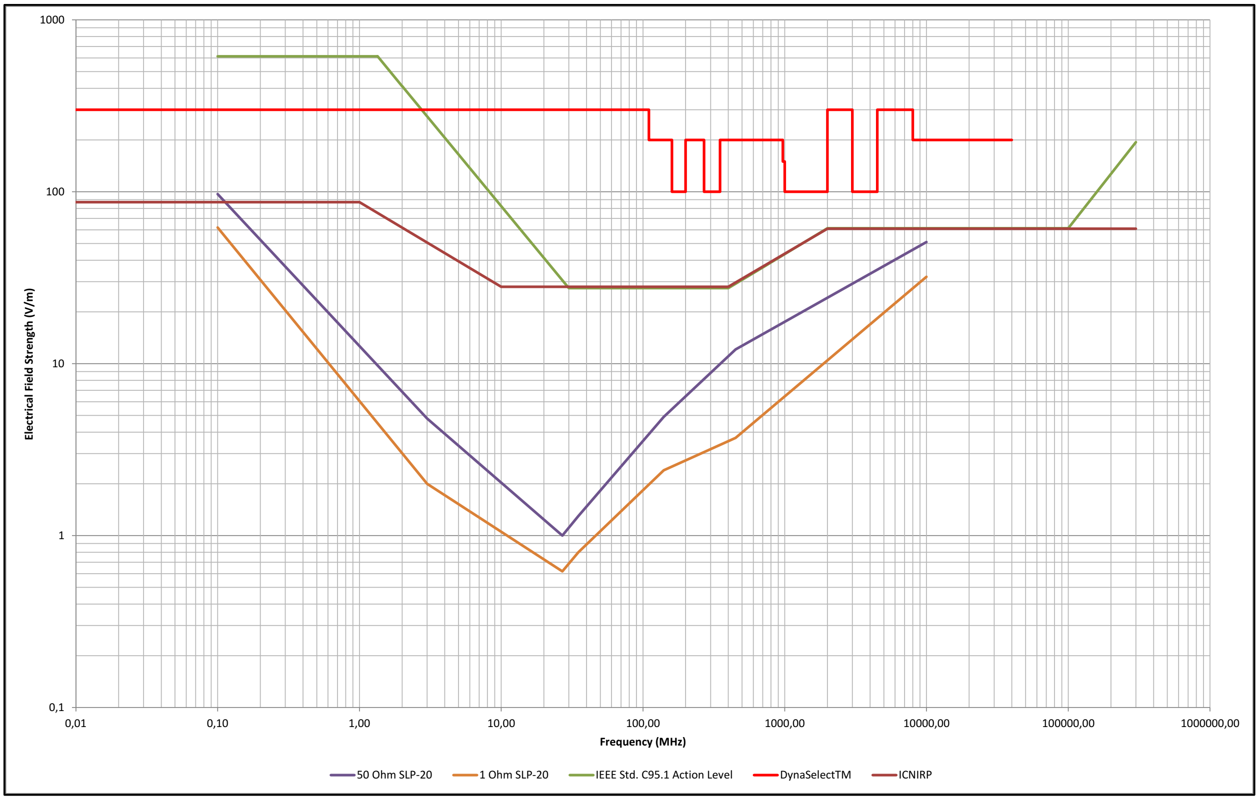

Fig. 3. Electronic detonators measurement results.

In Fig. 3, the red curve at the top shows the measurement results for electronic detonators. These detonators are insensitive to electromagnetic (EM) radiation at field strengths of 300 V/m in the frequency range between 100 kHz and 100 MHz. In the frequency range of 100 MHz to 4.5 GHz, the electronic detonators are insensitive to a field strength of 100 V/m. At frequency levels higher than 4.5 GHz, the insensitive field strength levels vary between 100 and 300 V/m.

As a comparison or for ease of reference, the curves from electrical (1-Ohm and 50-Ohm) detonators, the IEEE C95.1 action level and the ICNIRP are included on the diagram.

Safety-Distance Calculations. IME SLP 20 publishes eight separate tables that detail safe distances for 50-Ohm oilfield electric detonators[4].

The far-field formula, or far-induction field, was used to apply the data from the SLP 20 tables to calculate the safety distances from the authors' detonators to transmission equipment. Using the near-field formula would have provided a far more unfavorable result, yet from a safety aspect, this methodology provides an additional safety factor in the calculations.

The **safe-distance calculation**, with known field strength, is derived from the formula for the calculation of power density[5].

$$S = \frac{P \cdot G}{4\pi D^2} \qquad (1)$$

$$S = \frac{E^2}{Z_0} \qquad (2)$$

- S = power density [W/m²]
- P = transmitter power [W]
- G = factor of antenna gain

- D = distance [m]
- E = field strength [V/m]
- Z_0 = impedance of free space [Ω] = 377 Ω

The **effective isotropic radiated power** [W] is defined with[6]:

$$EIRP = P \cdot G \qquad (3)$$

Combining all three equations:

$$\frac{E^2}{Z_0} = \frac{EIRP}{4\pi D^2} \qquad (4)$$

The **distance for an effective isotropic radiated power** is defined with:

$$D = \frac{\sqrt{30 \cdot EIRP}}{E} \qquad (5)$$

The **effective radiated power** [W] is defined[7]:

$$ERP = EIRP \cdot 1{,}64 \qquad (6)$$

For the **effective radiated power**, the distance formula is defined[8]:

$$D = \frac{7{,}02\,\sqrt{ERP}}{E} \qquad (7)$$

Because of the calculation with the free space impedance of 377 Ω, this formula is especially for the far-field. The **beginning of the far-field** is defined with the below formula. Λ = wavelength [m].

$$\frac{\lambda}{2\pi} \qquad (8)$$

The electrical field strength calculation in the near-field is complex because the electrical free space impedance increases depending on distance and antenna configuration. For an exact calculation in the near-field, complex models of every possible antenna configuration would have to be created.

For electrical field strength, the near-field calculation would deliver more precise results with lower values because of the increasing free-space impedance.
For this reason, the far-field formula was also used in the near-field to calculate safe distances. Because these calculated distances tended to be larger, an additional worst-case scenario was generated.

In general, the safe-distance calculation is a worst-case scenario, because influence factors (i.e., mast height, ground obstacles, antenna alignment, etc.), which decrease field strength, are not observed or taken into consideration. The safe-distance calculation is always performed with the maximum possible field strength.

Example of a calculation. Using the previous distance formula, the safety distance D, as shown in Fig. 4, can be calculated for each transmission power of the corresponding transmitter, and likewise by applying the corresponding field strength in the formula.

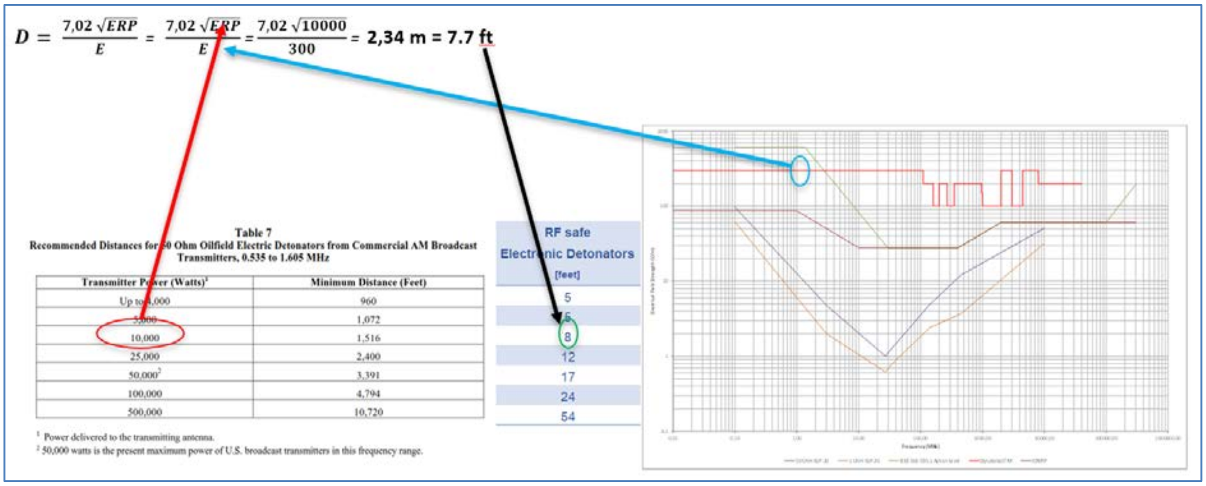

$$D = \frac{7{,}02\sqrt{ERP}}{E} = \frac{7{,}02\sqrt{ERP}}{E} = \frac{7{,}02\sqrt{10000}}{300} = 2{,}34\ \mathrm{m} = 7.7\ \mathrm{ft}$$

Table 7
Recommended Distances for 50 Ohm Oilfield Electric Detonators from Commercial AM Broadcast Transmitters, 0.535 to 1.605 MHz

Transmitter Power (Watts)[1]	Minimum Distance (Feet)
Up to 4,000	960
5,000	1,072
10,000	1,516
25,000	2,400
50,000[2]	3,391
100,000	4,794
500,000	10,720

[1] Power delivered to the transmitting antenna.
[2] 50,000 watts is the present maximum power of U.S. broadcast transmitters in this frequency range.

RF safe Electronic Detonators [feet]
5
5
8
12
17
24
54

Fig. 4. Calculation for safety distance D.

To illustrate the dramatic decrease in minimum safe distance achieved by selecting the electronic detonators, a comparison to a 50-Ohm oilfield detonator was performed for each transmitter type tested by IME. The results are provided below, in Tables 1 through 8, using original data from the corresponding SLP 20 table as a reference. All of these include electronic detonator distances.

Table 1. AM Broadcast Transmitter (0.535 to 1.605 MHz) From SLP 20, Table 7

Antenna Gain*	1
Measured Field Strength 0.535 to 1.605 MHz	300 V/m

	Recommended Minimum Distance	
Transmitter Power [Watt]	**50 Ohm Oilfield Electric Detonators [feet]**	**RF safe Electronic Detonators [feet]**
4,000	960	5
5,000	1,072	5
10,000	1,516	8
25,000	2,400	12
50,000	3,391	17
100,000	4,794	24
500,000	10,720	54

Values for 50 Ohm Detonators calculated at 1.6 MHz*

* Ref. IEEE Std. C95.4^{TM}-2002, Table 3 Note a

Table 2. Transmitters Up To 50 MHz From SLP-20, Table 8

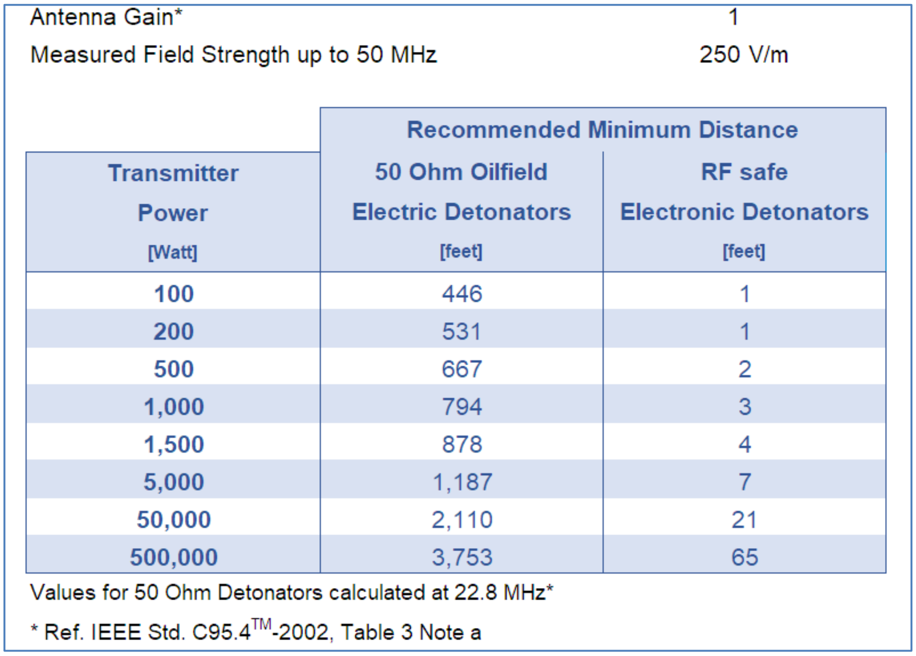

Antenna Gain*	1
Measured Field Strength up to 50 MHz	250 V/m

	Recommended Minimum Distance	
Transmitter Power [Watt]	**50 Ohm Oilfield Electric Detonators** [feet]	**RF safe Electronic Detonators** [feet]
100	446	1
200	531	1
500	667	2
1,000	794	3
1,500	878	4
5,000	1,187	7
50,000	2,110	21
500,000	3,753	65

Values for 50 Ohm Detonators calculated at 22.8 MHz*

* Ref. IEEE Std. C95.4^{TM}-2002, Table 3 Note a

Table 3. Mobile Transmitters From SLP 20, Table 9

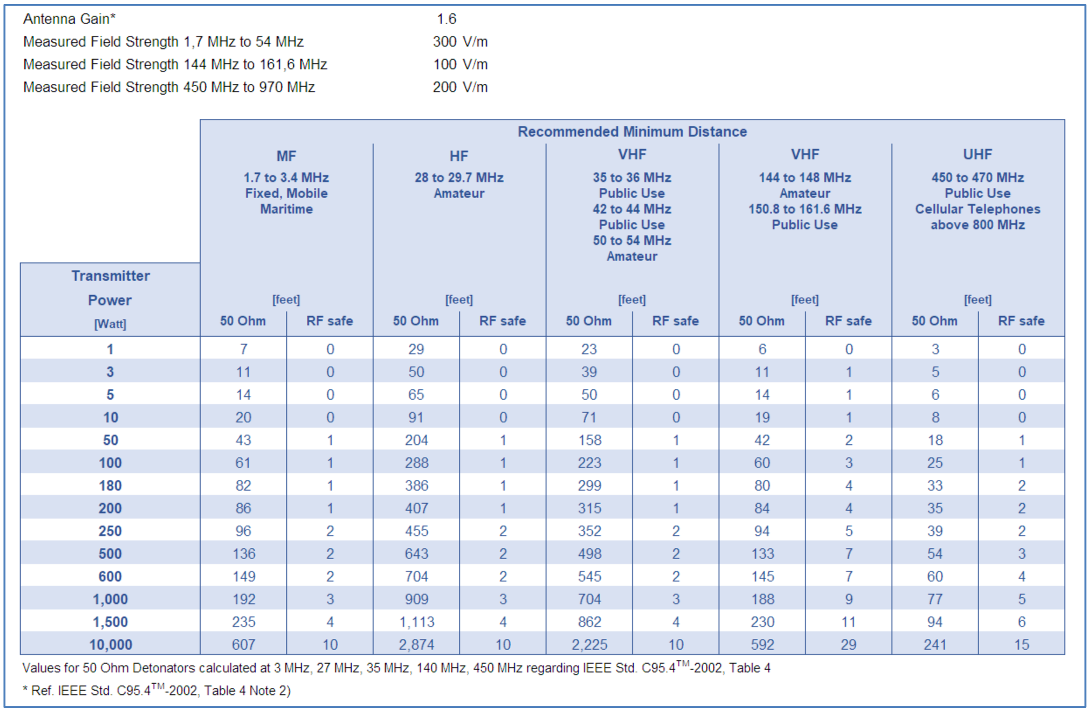

Antenna Gain*	1.6
Measured Field Strength 1,7 MHz to 54 MHz	300 V/m
Measured Field Strength 144 MHz to 161,6 MHz	100 V/m
Measured Field Strength 450 MHz to 970 MHz	200 V/m

	Recommended Minimum Distance									
	MF 1.7 to 3.4 MHz Fixed, Mobile Maritime [feet]		HF 28 to 29.7 MHz Amateur [feet]		VHF 35 to 36 MHz Public Use 42 to 44 MHz Public Use 50 to 54 MHz Amateur [feet]		VHF 144 to 148 MHz Amateur 150.8 to 161.6 MHz Public Use [feet]		UHF 450 to 470 MHz Public Use Cellular Telephones above 800 MHz [feet]	
Transmitter Power [Watt]	**50 Ohm**	**RF safe**	**50 Ohm**	**RF safe**	**50 Ohm**	**RF safe**	**50 Ohm**	**RF safe**	**50 Ohm**	**RF safe**
1	7	0	29	0	23	0	6	0	3	0
3	11	0	50	0	39	0	11	1	5	0
5	14	0	65	0	50	0	14	1	6	0
10	20	0	91	0	71	0	19	1	8	0
50	43	1	204	1	158	1	42	2	18	1
100	61	1	288	1	223	1	60	3	25	1
180	82	1	386	1	299	1	80	4	33	2
200	86	1	407	1	315	1	84	4	35	2
250	96	2	455	2	352	2	94	5	39	2
500	136	2	643	2	498	2	133	7	54	3
600	149	2	704	2	545	2	145	7	60	4
1,000	192	3	909	3	704	3	188	9	77	5
1,500	235	4	1,113	4	862	4	230	11	94	6
10,000	607	10	2,874	10	2,225	10	592	29	241	15

Values for 50 Ohm Detonators calculated at 3 MHz, 27 MHz, 35 MHz, 140 MHz, 450 MHz regarding IEEE Std. C95.4^{TM}-2002, Table 4

* Ref. IEEE Std. C95.4^{TM}-2002, Table 4 Note 2)

Table 4. Citizen’s Band, Class D Transmitters (26,965 to 27,405 MHz) from SLP 20, Table 9a

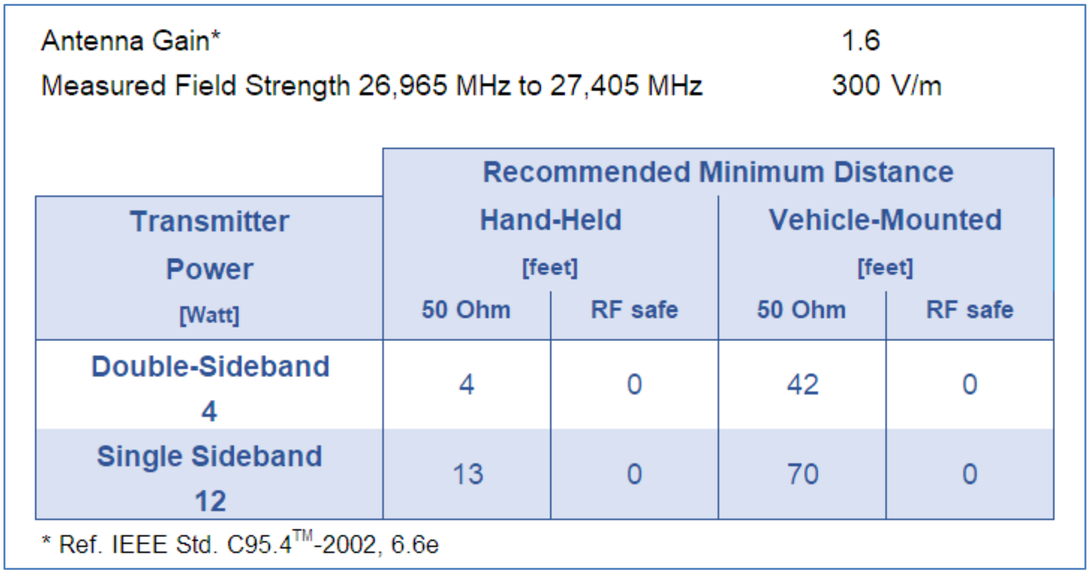

Antenna Gain* 1.6
Measured Field Strength 26,965 MHz to 27,405 MHz 300 V/m

Transmitter Power [Watt]	Recommended Minimum Distance Hand-Held [feet] 50 Ohm	 Hand-Held [feet] RF safe	 Vehicle-Mounted [feet] 50 Ohm	 Vehicle-Mounted [feet] RF safe
Double-Sideband 4	4	0	42	0
Single Sideband 12	13	0	70	0

* Ref. IEEE Std. C95.4$^{\text{TM}}$-2002, 6.6e

Table 5. VHF TV and FM Broadcasting Transmitters (54 to 216 MHz) from SLP 20, Table 10

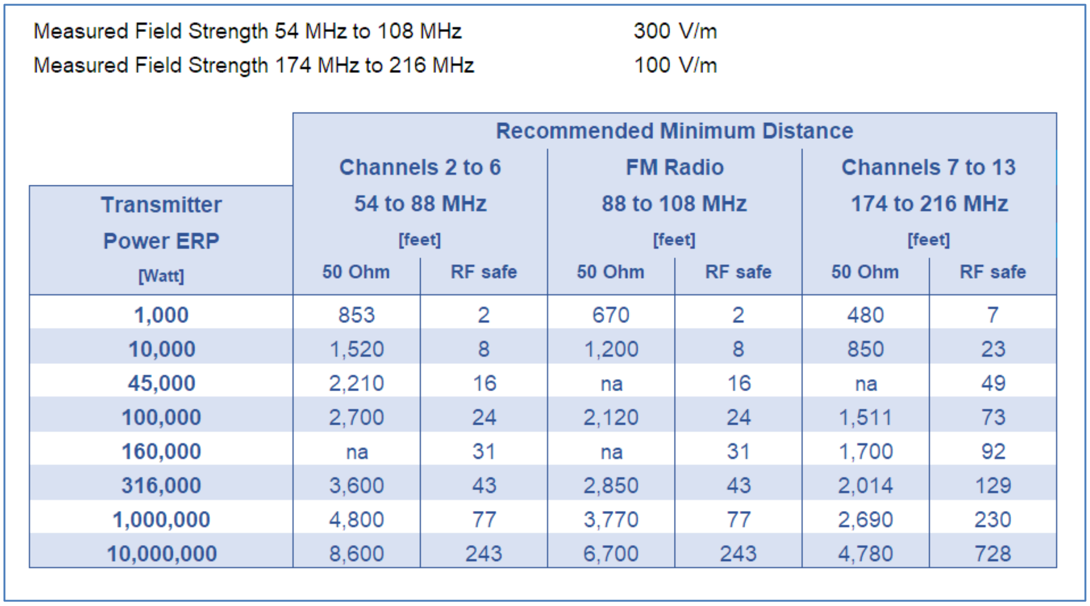

Measured Field Strength 54 MHz to 108 MHz 300 V/m
Measured Field Strength 174 MHz to 216 MHz 100 V/m

Transmitter Power ERP [Watt]	Recommended Minimum Distance Channels 2 to 6 54 to 88 MHz [feet] 50 Ohm	 Channels 2 to 6 54 to 88 MHz [feet] RF safe	 FM Radio 88 to 108 MHz [feet] 50 Ohm	 FM Radio 88 to 108 MHz [feet] RF safe	 Channels 7 to 13 174 to 216 MHz [feet] 50 Ohm	 Channels 7 to 13 174 to 216 MHz [feet] RF safe
1,000	853	2	670	2	480	7
10,000	1,520	8	1,200	8	850	23
45,000	2,210	16	na	16	na	49
100,000	2,700	24	2,120	24	1,511	73
160,000	na	31	na	31	1,700	92
316,000	3,600	43	2,850	43	2,014	129
1,000,000	4,800	77	3,770	77	2,690	230
10,000,000	8,600	243	6,700	243	4,780	728

Table 6. UHF TV transmitters (470 to 806 MHz) from SLP 20 Table 11, including the authors' electronic detonator distances.

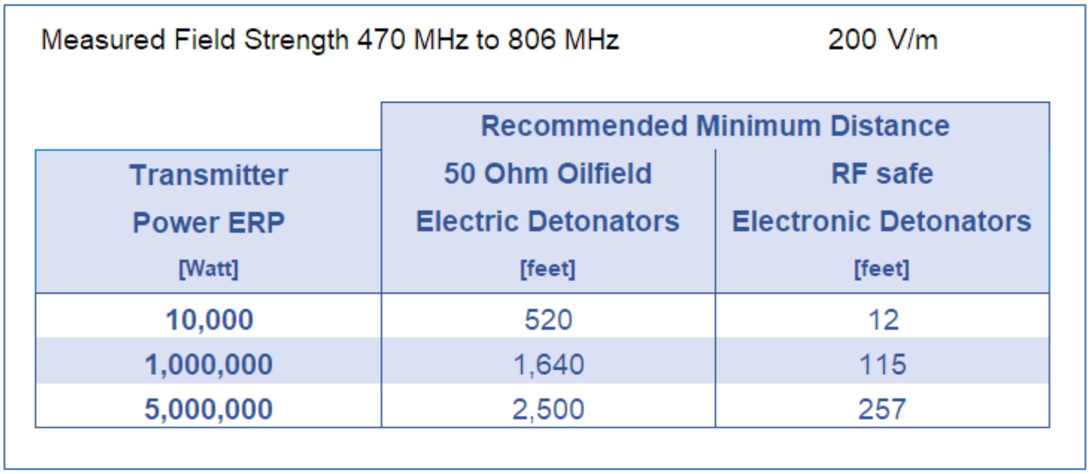

Measured Field Strength 470 MHz to 806 MHz 200 V/m

Transmitter Power ERP [Watt]	Recommended Minimum Distance 50 Ohm Oilfield Electric Detonators [feet]	 RF safe Electronic Detonators [feet]
10,000	520	12
1,000,000	1,640	115
5,000,000	2,500	257

Table 7. Maritime Navigational Radar (5.99 to 9.99 GHz) from SLP 20, Table 12

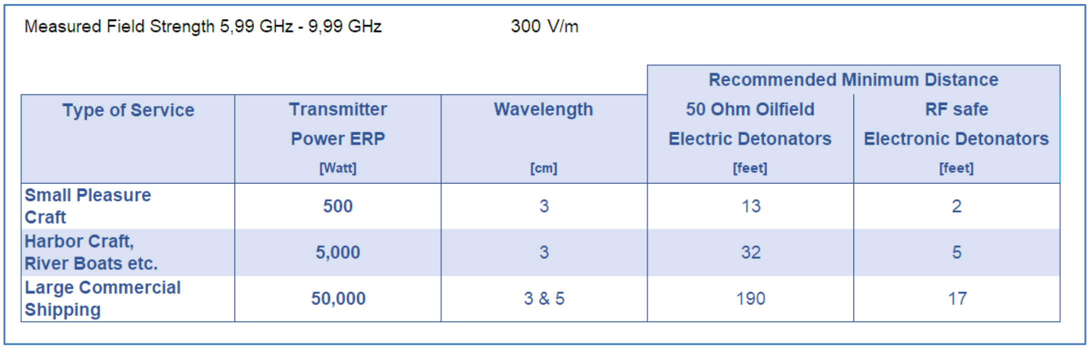

Measured Field Strength 5,99 GHz - 9,99 GHz 300 V/m

Type of Service	Transmitter Power ERP [Watt]	Wavelength [cm]	Recommended Minimum Distance 50 Ohm Oilfield Electric Detonators [feet]	 RF safe Electronic Detonators [feet]
Small Pleasure Craft	500	3	13	2
Harbor Craft, River Boats etc.	5,000	3	32	5
Large Commercial Shipping	50,000	3 & 5	190	17

Table 8. Radio Navigation Beacon (0.1 to 315 MHz) from SLP 20, Table 12a

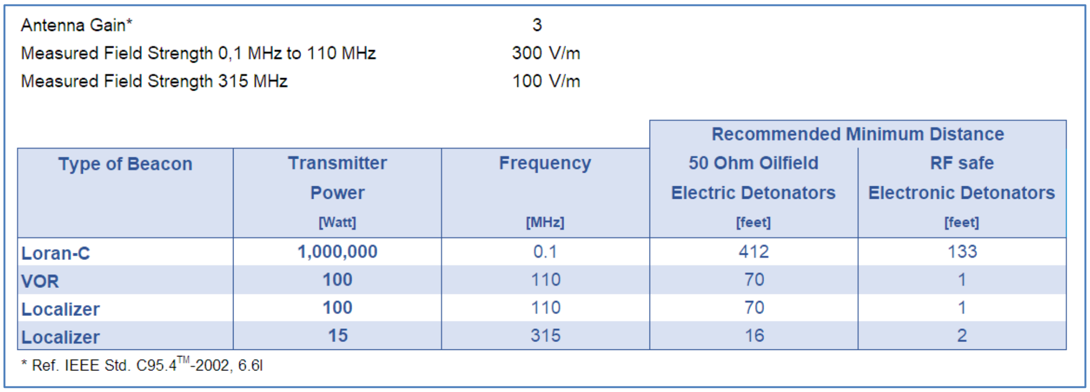

Antenna Gain*	3
Measured Field Strength 0,1 MHz to 110 MHz	300 V/m
Measured Field Strength 315 MHz	100 V/m

Type of Beacon	Transmitter Power [Watt]	Frequency [MHz]	Recommended Minimum Distance 50 Ohm Oilfield Electric Detonators [feet]	 RF safe Electronic Detonators [feet]
Loran-C	1,000,000	0.1	412	133
VOR	100	110	70	1
Localizer	100	110	70	1
Localizer	15	315	16	2

* Ref. IEEE Std. C95.4$^{\text{TM}}$-2002, 6.6l

Sample calculation for multiple RF transmitters. According to API RP 67 fourth edition, § 7.3.6.2.4.1, sample calculations must be conducted with 100 handheld 5-watt transmitters plus 20 mobile 200-watt transmitters, each set at 144 MHz or higher (the most sensitive frequency). All 5-watt transmitters must be the same distance apart, and all 200-watt transmitters must be the same distance apart.

Assumption. The handheld transmitters were placed in a circular arrangement around the detonator to achieve equal distance between the detonator and transmitters. A group of 100 people each holding a transmitter were spaced 1m apart, resulting in a circumference of 100m. This provides a radius of 15.9m.

The 200-watt effective radiated power (ERP) mobile transmitters are industrial-grade and mounted in vehicles. To achieve equal distance to the detonator, the vehicles were arranged in a circle with the detonator in the center.

Assuming a truck width of 3m and leaving 1m space between each truck, this test requires 20 trucks with a circumference of 80m. This results in a radius of 12.7m.
Calculation at frequency 160 MHz (most sensitive frequency) with E4 max of 100 V/m. Handheld transmitters T1 to T100, with 15.9m, results in field strengths for E1 to E100 of 0.98 V/m. Mobile transmitters T101 to T120, with a distance of 12.7m, results in field strengths for M101 to M120 of 7.7 V/m. Result = 0.128 < 1.

$$\left(\frac{E1}{E4max}\right)^2 + \left(\frac{E2}{E4max}\right)^2 + \left(\frac{E3}{E4max}\right)^2 + \cdots + \left(\frac{E120}{E4max}\right)^2 < 1 \qquad (8)$$

The sum of field strengths of the multiple transmitters is below the *maximum acceptable electric field strengths* for the electronic detonator.

3. Summary

The safe distances for the 50-Ohm resistorized detonators were previously measured and empirically tested by the IME. The authors' electronic RF-safe detonators were measured in a laboratory environment to check for induced current at the fuse head due to electromagnetic radiation under the worst-case scenarios, across a range of frequencies and field strengths. A table of safe distances was established by using the measurements of induced current in a safe-state and applying calculations for the range of frequency values and electromagnetic field-strength values.

As expected, the safe distances were significantly shorter for the RF-safe electronic detonators, as compared to the 50-Ohm resistorized detonators, allowing them to be used on tight wellsite footprints.

According to the measurements made, the resistorized detonators tested herein were found to fulfill the Group 1 requirements, according to the API RP 67 fourth edition, and a table of safety distances is available. The RF-safe electronic detonators tested herein were found to fulfill the Group 2 requirements. Sample calculations of the RF-exclusion distances for multiple RF transmitters are provided, and tables of the safe distances for each individual transmitter type (according to SLP 20) have been determined.

References

1. API RP-67 Recommended Practice for Oilfield Explosives, First Edition, March 1, 1994, http://www.demex.us/ReferenceMaterial/OperationalReference/Recommended%20Practices%20for%20Oilfield%20Explosives%20Safety.pdf
2. PHMSA Hazardous Materials Regulations, https://www.phmsa.dot.gov/standards-rulemaking/hazmat/hazardous-materials-regulations
3. Ayre,D. and Barker, J., API RP 67 Oilfield Explosive Safety: Proposed Changes for the 4th Edition, Perforators.org, May 16, 2016 https://www.perforators.org/wp-content/uploads/2016/05/IPS-16-01.pdf
4. SLP20: Safety Guide for the Prevention of Radio Frequency Radiation Hazards in the Use of Commercial Electric Detonators (Blasting Caps), https://www.ime.org/products/details/slp20
5. Franklin Applied Physics, James G. Stuart, Ph.D., Radio Frequency Sensitivity Of Electronic Detonators March 2016 Report 20794-06, Page 11 of 18
6. BGR GUV Rule 241 for Blasting Work, https://www.umwelt-online.de/recht/arbeitss/uvv/bgr/241_ges.htm
7. Effective radiated power, Wikipedia, https://en.wikipedia.org/wiki/Effective_radiated_power
8. Field strength vs. radiated power, PROCOM A/S, http://www.parc.org.za/publications/=Field%20strength%20vs%20radiated%20power.pdf

PERFORATORS.ORG
INTERNATIONAL PERFORATING FORUM